Water Resources Research

RESEARCH ARTICLE
10.1029/2025WR041074

Rapid Fault Leakage Modelling for CO_2 Storage in Saline Aquifers

Hariharan Ramachandran[1], Iain de Jonge-Anderson[1], Ikhwanul Hafizi Musa[2], Uisdean Nicholson[1], Chee Phuat Tan[3,4], Sebastian Geiger[5], and Florian Doster[1]

[1]Institute of GeoEnergy Engineering, Heriot-Watt University, Edinburgh, UK, [2]PETRONAS Research Sdn Bhd, Bangi, Malaysia, [3]PETRONAS Carigali Sdn Bhd, Kuala Lumpur, Malaysia, [4]EJ Geomechanics Consulting, Kuala Lumpur, Malaysia, [5]Department of Geoscience and Engineering, Delft University of Technology, Delft, The Netherlands

Key Points:

- Modeling approach combining vertical equilibrium with a new fault leakage function for computationally efficient CO_2 storage risk assessment
- Framework integrates fault-specific properties, such as capillary entry pressure and permeability, to improve predictions of leakage risks
- This tool supports early stage site screening, fault risk mitigation, and scalable deployment of CO_2 storage projects

Correspondence to:
H. Ramachandran,
h.ramachandran@hw.ac.uk

Citation:
Ramachandran, H., de Jonge-Anderson, I., Hafizi Musa, I., Nicholson, U., Tan, C. P., Geiger, S., & Doster, F. (2026). Rapid fault leakage modelling for CO_2 storage in saline aquifers. *Water Resources Research*, *62*, e2025WR041074. https://doi.org/10.1029/2025WR041074

Received 19 MAY 2025
Accepted 23 MAR 2026

Author Contributions:
Conceptualization: Hariharan Ramachandran, Chee Phuat Tan, Sebastian Geiger, Florian Doster
Data curation: Iain de Jonge-Anderson, Ikhwanul Hafizi Musa, Uisdean Nicholson
Formal analysis: Hariharan Ramachandran, Iain de Jonge-Anderson, Ikhwanul Hafizi Musa, Uisdean Nicholson, Florian Doster
Funding acquisition: Sebastian Geiger, Florian Doster
Investigation: Hariharan Ramachandran, Iain de Jonge-Anderson, Uisdean Nicholson, Sebastian Geiger, Florian Doster
Methodology: Hariharan Ramachandran, Sebastian Geiger, Florian Doster
Project administration: Chee Phuat Tan, Florian Doster

Abstract Simulating the fluid flow along fault zones at different scales is essential for predicting the CO_2 leakage and containment during injection and storage. However, this can be challenging, especially in the early stages of a storage project when knowledge of the reservoir and caprock is limited and the cost of obtaining the relevant data is high. This study develops a tool for fast screening of fault leakage at the site screening stage. The tool uses a vertically integrated reservoir model coupled with a newly developed upscaled fault leakage function based on source/sink relations. The fault is conceptualized as an increased vertical permeability through the caprock due to the presence of a fracture network in the damage zone and a reduced horizontal permeability in the reservoir due to fault throw and presence of a low-permeability fault core. The proposed tool is validated against numerical simulations demonstrating strong agreement in predicting leakage rates under varying reservoir conditions. The model's capabilities are further tested through simulation cases, including a field-scale application in the Malay Basin. These cases revealed key insights into the roles of fault permeability and fault capillary entry pressure in controlling leakage and highlighted the importance of accurately characterizing these properties to mitigate risks. The computationally efficient model presented in this study is a valuable tool for quantifying uncertainties in key fault parameters, and other constitutive relations that affect the behavior of the storage reservoir and potential fault leakage.

1. Introduction

Storing CO_2 in geological formations is a crucial method for mitigating climate change and will be an essential component of a Net Zero Carbon Emission energy landscape in the coming decades (Hepple & Benson, 2005; Krevor et al., 2023). Among the most attractive storage options are saline aquifers, which are widely distributed and possess substantial total storage capacities exceeding gigatons of CO_2 globally (Celia et al., 2015; Herzog, 2011; Kumar et al., 2005). However, successful implementation hinges on the long-term secure containment of CO_2 within these aquifers. Leakage undermines mitigation efforts, poses environmental/health risks, and can erode public trust in Carbon Capture and Storage (CCS) (Ashworth et al., 2015; Bielicki et al., 2014; Jones et al., 2015). Regulatory bodies emphasize the importance of comprehensive geological characterization and storage site assessment to identify significant leakage risk (Anderson, 2017; Climate Change Committee, 2021; Dixon et al., 2015; Romanak & Dixon, 2022). In this context, faults play a crucial role as they can either increase or reduce storage potential, depending on host and fault rock properties. In some cases, by juxtaposing impermeable rock layers, they can function as structural traps, confining the injected CO_2 (Knipe et al., 1998; Pei et al., 2015). Conversely, faults also possess the potential to act as leakage pathways that connect the storage reservoir through the overlying caprock to shallower geological layers (Bachu, 2008; Rutqvist, 2012; Snippe et al., 2022). As the scale of CCS deployment increases, we will encounter numerous storage formations containing faults, some of which may be sub-seismic, with uncertain properties. To expedite the storage site screening, rapid assessment tools are needed to screen for fault-related leakage risks during the early stages of project development.

Faults are complex zones of deformation characterized by a central zone of intensely sheared rock, referred to as the fault core, surrounded by a fractured damage zone with a progressively decreasing fracture density with increasing distance from the fault core (Figure 1) (Childs et al., 2009; Faulkner et al., 2010; Gillespie et al., 1993; Ketterman et al., 2020; Phillips et al., 2020; Sibson, 1977; Walsh et al., 1998). The fault core typically exhibits relatively low permeability because of cataclasis or clay smear (Ballas et al., 2015; Bense & Person, 2006;

Resources: Iain de Jonge-Anderson, Ikhwanul Hafizi Musa, Uisdean Nicholson, Chee Phuat Tan
Software: Hariharan Ramachandran
Supervision: Sebastian Geiger, Florian Doster
Validation: Hariharan Ramachandran, Florian Doster
Visualization: Hariharan Ramachandran, Iain de Jonge-Anderson
Writing – original draft: Hariharan Ramachandran
Writing – review & editing: Iain de Jonge-Anderson, Ikhwanul Hafizi Musa, Uisdean Nicholson, Chee Phuat Tan, Sebastian Geiger, Florian Doster

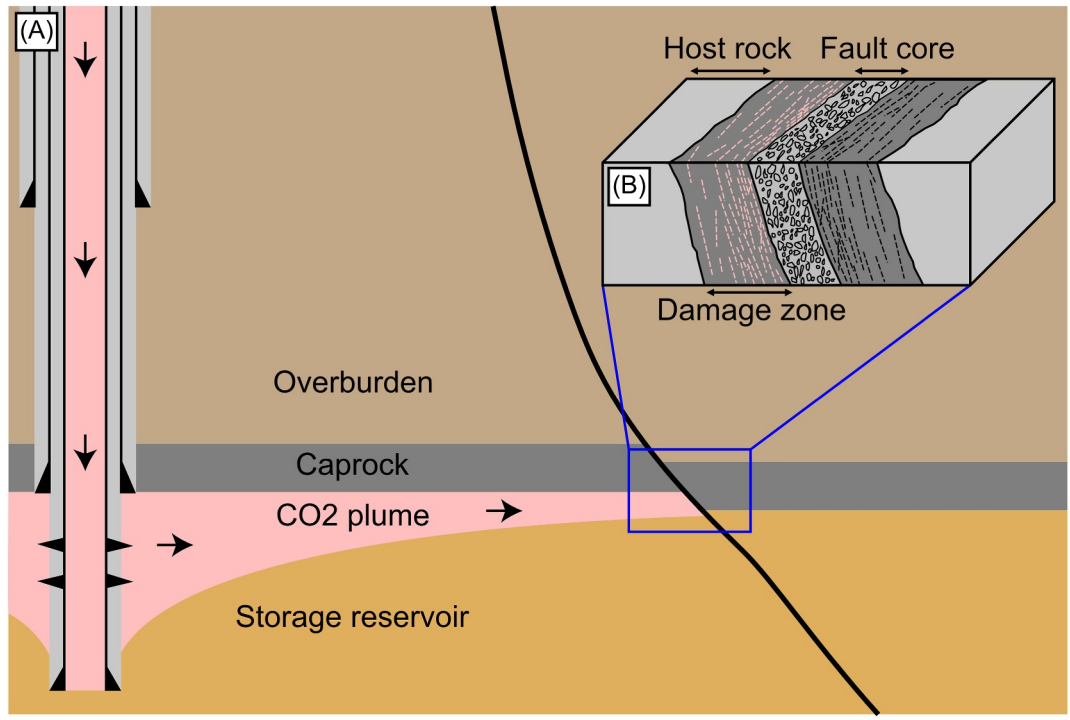

Figure 1. An illustrative representation of CO_2 storage in a faulted reservoir-caprock system. CO_2 is injected into permeable rock layers spanning hundreds of meters in thickness, with a low-permeability regional seal acting as the primary caprock. The presence of faults can either result in enhanced entrapment or vertical leakage, depending on fault properties (a). Schematic illustration of fault zone properties, including the fault core and adjacent damage zone (b). Figure adapted from Gasda et al. (2022).

Dewhurst et al., 2018; Tueckmantel et al., 2012), while the associated damage zones, dominated by fractures, can exhibit permeabilities several orders of magnitude greater, which can increase their leakage potential (Caine et al., 1996; Childs et al., 2009; Seebeck et al., 2014). The critical fault properties controlling leakage through faulted zones include fault geometry, architecture, stress regime, and fracture density, among several others (Gibson, 1998; Rizzo et al., 2024; Rutqvist, 2012; Smith, 1980; Yielding et al., 2010). Additionally, fault reactivation due to injection-induced changes in pore pressure and stress conditions can potentially generate new leakage pathways/fractures or alter existing ones (Tewari et al., 2023). Seismic imaging resolution limits the characterization of fine-scale features within the damage zone introducing uncertainties, as their presence, properties, and ability to form interconnected networks at larger scales remain poorly understood (Rizzo et al., 2024). This limited knowledge, particularly during the early stages of a CCS project when reservoir data is scarce and data acquisition expensive, can significantly hinder informed decision-making (Oladyshkin et al., 2011; Pawar et al., 2015, 2016). Additionally, operators typically assess multiple potential storage sites in their portfolio, necessitating efficient screening methods to identify the most suitable storage candidates. This study focuses on pre-existing permeable fault zones and does not model fault reactivation or geomechanical-dynamic coupling. We consider these faults zones as a potential leakage pathway whose flow behavior must be characterized. Stress-induced permeability changes, fault slip, and pressure-stress coupling are critical processes for comprehensive CCS risk assessment (Chang & Segall, 2016; Chen et al., 2024; Jha & Juanes, 2014; Meguerdijian and Jha, 2021; Rinaldi et al., 2014; Zhao and Jha, 2019) but require detailed site-specific geomechanical data rarely available during early stage screening. These processes are best addressed through coupled geomechanical-dynamic models during later stages of site evaluation. However, by evaluating leakage across a wide uncertainty range of fault permeabilities—including values that may result from mechanical processes—allows our screening approach to bound potential risks without explicitly modeling the underlying mechanisms.

Reservoir simulation plays a vital role in quantifying potential fault leakage rates for large-scale CO_2 storage modeling. In the context of this study, fault leakage refers to the upward migration of CO_2 along fault zones,

driven by pressure gradients and buoyancy forces. This process occurs when faults act as vertical conduits, connecting storage reservoirs to overlying formations or the surface, potentially compromising the integrity of CO_2 containment. The implementation of faults in full reservoir simulations is typically limited to transmissibility multipliers, which adjust flow properties between adjacent grid blocks to reflect across fault permeability (Manzocchi et al., 1999). These multipliers cannot capture the interplay between fault permeability and vertical pressure gradients, and the overlying formations need to be explicitly gridded increasing the computation requirements of the model and limiting their applicability for detailed fault risk assessment. Moreover, faults and damage zones are significantly smaller than the grid cells employed in typical field-scale simulations necessitating either fine-scale gridding or local grid refinement around the fault zone to resolve their behavior. While several workflows with detailed models that incorporate complex fault geometries, rock properties, explicitly gridded overlying formations and multiphase flow dynamics to capture the interplay between CO_2 migration, leakage, and pressure changes, the computational demands associated with such models can be prohibitive (Bjornara et al., 2023; Fachri et al., 2013; Gasda et al., 2022; Jha & Juanes, 2014; Silva et al., 2023; Snippe et al., 2022). This is especially true when considering uncertainties in subsurface data and the need for multiple simulations (scenario analyses) (Ringrose and Bentley, 2021). Sub-seismic faults, which are undetectable in seismic data, exacerbate modeling uncertainties due to their poorly constrained geometry, permeability, and potential connectivity (Childs et al., 2009; Yielding et al., 1997). Reservoir modeling to account for such complexities requires days to weeks to run, limiting its utilization for early stage site screening. These limitations underscore the urgent need for fast and efficient modeling tools that can evaluate fault-related leakage risks, support site selection, and identify risk mitigation strategies and monitoring plans in CCS projects. To address these limitations, this study introduces a simplified analytical fault leakage function that captures vertical flow dynamics within fault zones while avoiding the computational costs associated with explicit fault gridding or fine-scale modeling. The approach is explicitly designed for screening as it identifies which fault parameters and geological scenarios warrant detailed investigation, rather than attempting to forecast fault mechanisms.

Vertical equilibrium (VE) models have been developed to simplify three-dimensional multiphase flow simulations by leveraging two key characteristics of CO_2 storage systems: the strong buoyancy of CO_2 relative to brine and the significantly larger horizontal dimensions compared to the vertical dimension of the reservoir (Huppert & Woods, 1995; Nordbotten and Celia, 2011; Yortsos, 1995). These characteristics promote rapid CO_2 separation and vertical equilibrium within the reservoir. VE flow models exploit this phenomenon by enabling the representation of the 3D reservoir system using a set of 2D governing equations, thereby significantly reducing computational costs. Several CO_2 storage studies have demonstrated that VE simulations yield results comparable to those obtained from 3D simulations for benchmark and field-scale problems (Bandilla et al., 2014; Class et al., 2009; Moyner & Nilsen, 2019; Nilsen et al., 2011, 2015, 2016a, 2016b). The basic formulation of VE models assumes a sharp interface between CO_2 and brine and keeps the mathematical structure of the standard multi-phase Darcy equation. Hence, conventional simulators can be used. This very characteristic allows for their expansion to encompass a wider range of complex phenomena. Recent research has successfully incorporated and evaluated various physical effects within VE models, including: (a) capillarity – the presence of non-negligible capillary pressure leads to the formation of a capillary fringe, a transition zone between the CO_2 and brine phases, rather than a sharp interface (Nilsen et al., 2015; Nordbotten & Dahle, 2011); (b) residual trapping and hysteresis – these intrinsic properties of the rock can significantly influence the distribution and flow of fluids within the reservoir (Doster et al., 2012, 2013; Du Plessis et al., 2013; Nilsen et al., 2016a, 2016b; Nordbotten & Celia, 2011); (c) dissolution of CO_2 into reservoir brine (Gasda et al., 2011; Nilsen et al., 2016a, 2016b); (d) compressibility of CO_2 in the vertical extent (Andersen et al., 2015); (e) thermal effects (Gasda et al., 2013); (f) simplified geomechanics (Andersen et al., 2016, 2017; Bjornara et al., 2016); (g) Hybrid-VE – using a coupled approach of mixing 3D and VE models which can help with simulating near-wellbore effects and multilayer reservoir modeling (Becker et al., 2017, 2018, 2022; Moyner & Nilsen, 2019). These advancements have demonstrated the ability of VE models to capture complex dynamics with comparable accuracy to 3D simulations, making them a suitable approach for computationally efficient assessment of field-scale CO_2 storage, especially for early stage projects which are subject to data uncertainty.

This study builds on these advancements by coupling a VE reservoir model with a newly developed fault leakage function to simulate vertical flow effects in faulted geological settings. We employ a VE flow model implemented within the open-source software package MRST-co2lab, which is a module within the MATLAB Reservoir Simulation Toolkit (MRST) (Andersen, 2017; Lie, 2019). The fault is conceptualized as an increased vertical

permeability through the caprock (due to the fracture network in the damage zone) while the horizontal permeability is reduced (due to throw and the presence of the fault core). Leakage rates are estimated using Darcy's law, considering the pressure differential across the layers connected by the fault. The flow is modeled as vertical single-phase flow along the fault. This simplification allows for a one-dimensional leakage system which lowers the cost of computation. The mathematical formulation of the proposed model is presented in Section 2, and the results are discussed in Section 3. The proposed modeling approach is demonstrated across four simulation cases presented in the results section.

The first case shows the verification of the upscaled fault leakage function against numerical simulations with explicitly gridded faults, demonstrating its accuracy in predicting along-fault leakage rates under varying fault permeability and capillary entry pressure conditions. The second case evaluates the model's robustness through convergence analysis across different grid resolutions and time step sizes, confirming its stability. The third case investigates the impact of capillary entry pressure using a sloping reservoir scenario, showing how increased capillary entry pressure delays leakage and reduces cumulative leakage rates. Finally, the model is applied to a field-scale CCS scenario in the Malay Basin, highlighting its efficiency and relevance for real-world fault leakage risk assessment.

2. Methods

This study examines the potential for $CO_{2\text{uiliveq}}$ storage within a faulted reservoir (Figure 1). We employ a vertically integrated numerical model for reservoir-scale flow coupled with an analytical model for fault leakage. A brief overview of the governing equations used in these models is presented in this section.

2.1. Vertical Equilibrium Modeling

The VE modeling approach for CO_2 storage is a simplification of traditional reservoir simulation methods that is particularly useful for large-scale CO_2 storage projects. This approach hinges on the assumption of VE, which posits that the buoyancy forces acting on the CO_2 cause it to segregate vertically much faster than it can migrate laterally. As a result, the CO_2 forms a thin layer beneath the caprock or under intermediate sealing layers, and the vertical pressure and fluid saturation distributions can be approximated by buoyancy and capillary forces. VE models reduce the dimensionality of the problem by vertically averaging the governing equations, which include conservation of mass and Darcy's law for fluid flow through porous media. This simplification results in a model that requires fewer grid cells and is computationally less intensive compared to full three-dimensional simulations. Post-simulation, the vertical pressure and fluid saturations can be reconstructed from the set of upscaled variables obtained by vertically integrating the conservation equations. Figure 2 illustrates the typical compression and reconstruction steps during a VE simulation at early and late times for an example simulation problem. This section provides a concise review of established equations for modeling flow in porous media and the VE simplification approach. For a more general and in-depth treatment of the derivations and the limits of the VE assumption, we refer the reader to the relevant literature (Nordbotten & Celia, 2011; Yortsos, 1995).

Consider the three-dimensional mass conservation equation for two immiscible and incompressible fluid phases α, CO_2 ($\alpha = g$) and brine ($\alpha = w$) as

$$\frac{\partial(\phi s_\alpha)}{\partial t} + \nabla \cdot u_\alpha = q_\alpha, \tag{1}$$

where ϕ is the porosity, s_α is the saturation of phase α, u_α is the Darcy velocity of phase α, and q_α is a source/sink term in units of volume of phase α per time. The porous medium is assumed to be rigid and under isothermal conditions. The volume balance is established by

$$s_g + s_w = 1. \tag{2}$$

The Darcy velocity of each phase is given by

$$\boldsymbol{u}_\alpha = -\frac{k_{r\alpha}}{\mu_\alpha}\boldsymbol{k}\left(\nabla p_\alpha - \rho_\alpha \boldsymbol{g}\right), \tag{3}$$

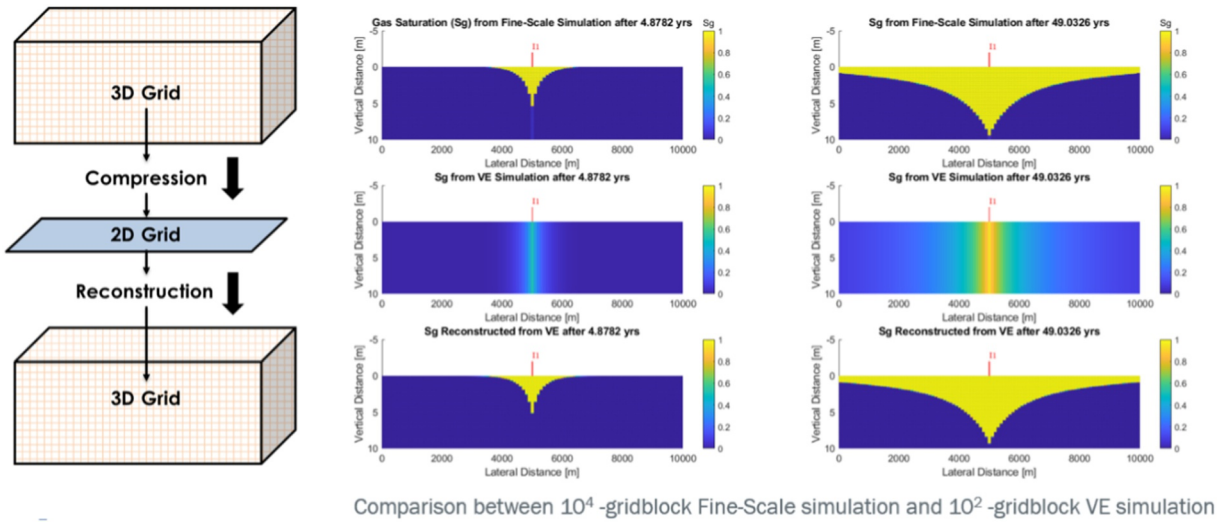

Figure 2. Illustration of the concept of VE model compression and reconstruction in a CO_2 injection simulation. The top panel shows an illustrative representation of the 3D simulation grid. The middle panel depicts the corresponding 2D grid generated by VE compression. The bottom panel presents the reconstructed 3D simulation grid obtained by solving the 2D VE model equations. These panels show the grid configuration at both early and late stages of the CO_2 injection simulation. In this example, the VE compression reduces a 10^4-cell 3D grid to a 10^2-cell VE grid, achieving significant computational efficiency without substantial information loss.

where μ_α is the viscosity of phase α, $k_{r\alpha}$ is the relative permeability of phase α, $\boldsymbol{k}$ is the permeability tensor, p_α is the fluid pressure of phase α, ρ_α is the density of phase α, and $\boldsymbol{g}$ is the gravity acceleration vector. The phase pressures are related by the capillary pressure function

$$p_c = p_g - p_w. \tag{4}$$

It is also assumed that the capillary pressure and relative permeability can be represented by algebraic functions. These functions depend solely on saturation and its history. Equations 1–4 form a set of 10 equations with 10 unknowns that need to be solved for in three dimensions. The fluid saturation distributions and pressures are obtained by solving this system, provided that: (a) specific functions are chosen to represent relative permeability and capillary pressure, (b) initial conditions for pressure and saturation throughout the reservoir are provided, and (c) appropriate boundary conditions are specified along the edges of the reservoir model.

In subsurface flow processes, the lateral dimension of interest is typically orders of magnitude larger (hundreds of meters to kilometers) compared to the vertical dimension (meters to tens of meters). This disparity leads to a more rapid redistribution of fluids vertically, allowing for the approximation of VE (Nordbotten & Celia, 2011; Nordbotten & Dahle, 2011). Consider a reservoir domain bounded by impermeable, horizontally oriented layers with a constant thickness H. The two fluids (brine and CO_2) are separated by a sharp interface within this reservoir. A cartesian coordinate system is employed, with the z-axis oriented in opposition to the gravitational vector (positive z upwards). Furthermore, for simplicity in the presentation here, constant permeability and porosity are assumed within the vertical direction, though VE is not limited to those assumptions (Nordbotten & Celia, 2011).

This vertical integration seeks to establish governing equations for the horizontal plane that utilize variables representing the average behavior throughout the reservoir thickness. Fine-scale quantities capture variations within the vertical dimension, while coarse-scale quantities represent the horizontally averaged behavior. Under the assumption of vertical hydrostatic equilibrium, Equation 3 indicates that the pressure gradient in each phase balances the gravity ($u_{\alpha z} = 0$). This characteristic allows for the determination of pressure at any vertical position by integrating the pressure from a reference level. To facilitate analysis, we normalize the z-axis with respect to the reservoir height H. Here, $z = 0$ is assigned to the bottom and $z = 1$ to the top of the reservoir. Consequently, the top of the reservoir is chosen as the reference position for pressure integration as

$$P_\alpha = p_\alpha(z = 1). \tag{5}$$

The reconstructed pressure is then given as

$$p_\alpha(z) = P_\alpha + \rho_\alpha g H(1 - z). \tag{6}$$

The other coarse-scale quantities are introduced by integrating the fine-scale quantities. This is done under the assumption of a homogeneous system with isothermal and incompressible fluids. We can obtain the coarse-scale equivalents after normalizing the vertical axis to the reservoir height and writing the equations in dimensionless form. For such systems, the coarse-scale equivalents of porosity Φ, permeability K, and viscosity M_α are simply a product of their respective fine-scale counterparts with reservoir height. This is because the averaging or integration process does not introduce any scaling factors in this case. The spatially dependent quantities are given as

$$S_\alpha = \frac{H}{\Phi} \int_0^1 \phi s_\alpha dz, \tag{7}$$

$$U_\alpha = H \int_0^1 u_\alpha dz, \tag{8}$$

$$K_{r\alpha} = \frac{H}{K} \int_0^1 k_{\|} k_{r\alpha}(s_\alpha(z))\, dz. \tag{9}$$

The subscript $\|$ denotes the variables in horizontal components such that U_α is a two-dimensional vector instead of three dimensions. With these definitions, Equations 1–4 after integrating over the vertical extent are given as

$$\frac{\partial(\Phi S_\alpha)}{\partial t} + \nabla_{\|} \cdot (U_\alpha) = Q_\alpha, \tag{10}$$

$$S_g + S_w = 1, \tag{11}$$

$$U_\alpha = -K \frac{K_{r\alpha}}{M_\alpha} \nabla_{\|} \mathrm{P}_\alpha, \tag{12}$$

$$P_c(\cdot) = P_g - P_w, \tag{13}$$

where $(\cdot)$ is used to highlight the upscaled dependence of the capillary pressure function that is yet to be determined. Equation 9 demonstrates that reconstructing the vertical, fine-scale saturation distributions, $s_w(z; x, y)$, is necessary to determine the effective parameter functions employed in a purely coarse-scale model. Fortunately, the assumption of hydrostatic fluid distribution facilitates this reconstruction process. By examining Equation 6, we observe that the fine-scale capillary pressure, $p_c(z; x, y)$, must compensate for the buoyancy force arising from the density difference. This relationship allows for the construction of the fine-scale capillary pressure and its subsequent connection to the coarse-scale capillary pressure as

$$p_c(z; x, y) = P_c(x, y) - \left(\rho_w - \rho_g\right) g H(1 - z). \tag{14}$$

A well-defined relationship between capillary pressure and water saturation enables the establishment of invertible $p_c - s_w$ mappings. These mappings allow for the reconstruction of the vertical saturation distribution, $s_w(z; x, y)$, given a specific coarse-scale capillary pressure P_c. Furthermore, Equation 7 can be employed to obtain a $P_c - S_w$ relationship. By leveraging this relationship, the fine-scale saturation distribution $s_w(z; x, y)$ is determined for a given coarse-scale saturation S_w. Consequently, coarse-scale relative permeabilities $K_{r\alpha}$ are dependent on coarse-scale saturations only.

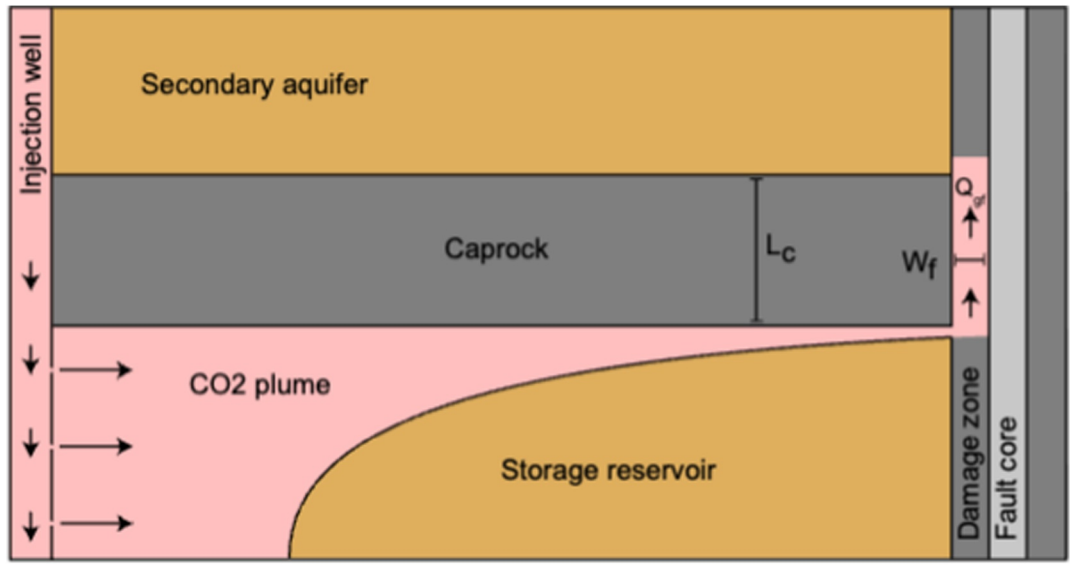

Figure 3. A schematic representation of a vertical cross-section of a storage reservoir containing a fault (gray). The black line represents the interface between the CO_2 and brine phases. CO_2 leaks along the damage zone of the fault after reaching the base of the fault within the reservoir.

2.2. Fault Leakage Function

This section details the steady-state analytical solution used to estimate leakage rates along the fault. The fault is conceptualized to connect the storage reservoir with a secondary aquifer at a shallower depth, which acts as sink for the leaking CO_2. Only faults of shorter lengths such that the CO_2 fluid properties remain nearly constant are considered here, while the long-range fault leakage (faults that connect the reservoir to the surface or seafloor) with variable CO_2 fluid properties and decompressive cooling has been investigated previously (Pruess, 2011; Ramachandran et al., 2017). The leaky fault is conceptualized as consisting of a low-conductivity (i.e., low permeability) core that could prevent flow across the fault. This core is surrounded by two high-conductivity (i.e., high-permeability) damage zones that permit flow vertically along the fault as shown in Figure 3 (Faulkner et al., 2010). This damage zone is referred to here as "the fault zone" or simply "the fault." This zone contains a low conductivity core that typically extends vertically into the reservoir. In this conceptualization, for the sake of simplicity, the flow across this low-conductivity core is represented as a no-flow boundary. However, it is important to note that flow across the core is typically represented using transmissibility multipliers (Manzocchi et al., 1999). Therefore, under this simplified no-flow assumption, fault leakage is conceptualized to occur upwards along the damage zone, which is modeled as an equivalent porous medium with representative rock properties.

This conceptualization embodies several key assumptions appropriate for early stage screening but not for detailed site characterization. We assume the fault damage zone is pre-existing and permeable, with permeability treated as constant rather than being stress-dependent. We do not model fault reactivation or injection-induced permeability evolution, processes that have been shown to significantly influence fault behavior and leakage dynamics during CO_2 injection (Jha & Juanes, 2014; Rinaldi et al., 2014; Rutqvist, 2012; Vilarrasa et al., 2017). These assumptions are appropriate for screening analyses evaluating scenarios where permeable pathways are assumed to exist. They are not appropriate for predicting whether faults will reactivate or for sites where critically stressed faults near failure are the primary concern for which coupled geomechanical-dynamic models are required (Chang & Segall, 2016; Meguerdijian and Jha, 2021; Zhao and Jha, 2019). The simplifications enable computational efficiency necessary for evaluating multiple sites and uncertainty realizations during initial screening, when detailed geomechanical data is unavailable and the goal is identifying sites warranting further investigation. This approach further allows exploration of fault permeabilities that lead to significant leakage and guides site prioritization for detailed assessment.

Estimating the hydraulic properties of the fault, particularly within the fault core and damage zone, is crucial for accurately modeling fault leakage. Fault zone permeabilities exhibit considerable variability depending on fault architecture, lithology, stress state, and deformation history. Fault zone permeabilities can range over 10 orders of magnitude, from 10^{-9} to 10^{-19} m^2 (Childs et al., 2009; Faulkner et al., 2010), with strong contrasts between different fault components. Specifically, fault cores exhibit relatively low permeability (10^{-17} to 10^{-21} m^2) due to cataclasis, clay smear, and gouge formation (Bense & Person, 2006; Rinaldi et al., 2014). In contrast, damage zones are typically several orders of magnitude more permeable and strongly depends on the nature of well-connected fracture networks (Caine et al., 1996; Faulkner et al., 2010; Rizzo et al., 2024). While insights can be gained from studying outcrop analogs, inherent uncertainties remain at the finer scale. Several researchers have developed stochastic modeling approaches to predict the fault properties, such as permeability, among other parameters (Berge et al., 2022; Gasda et al., 2022; Pettersson et al., 2025; Rizzo et al., 2024; Salo-Salgado et al., 2023). However, for this specific model, we are assuming constant fault properties throughout the simulation. The flow along the fault is described using Darcy's law by considering the pressure differential across the storage reservoir and the secondary aquifer, and the flow is assumed to occur only in the vertical direction. Once the CO_2 plume reaches the base of the fault within the aquifer, it is hypothesized to form a thick layer, acting as a barrier for aqueous phase entry into the fault (Kang et al., 2014). As a result, the aqueous flux along the fault is considered negligible and excluded from the function.

Several researchers have indicated that the CO_2 needs to overcome the capillary entry pressure of the fault, commonly referred to as the fault displacement pressure, for it to leak (Espinoza & Santamarina, 2017; Zheng & Espinoza, 2022). Fault capillary entry pressure depends on effective fracture aperture, wettability, and stress conditions. For intact caprocks, breakthrough pressures typically range from 0.5 to 5 MPa depending on lithology (Espinoza & Santamarina, 2017). However, fault damage zones with open fractures typically exhibit significantly lower entry pressures reflecting the larger effective apertures of fracture networks (Snippe et al., 2022; Zheng and Espinoza, 2022). For simplicity, we keep this parameter constant here. We base the flux calculation on the model presented by Neufeld et al. (2009) and Gilmore et al. (2022), with slight modifications to account for the reservoir overpressure caused by injection. This model describes leakage through fissures between two aquifers, with one being the targeted CO_2 storage site. We model the driving potentials ψ as

$$\psi = \Delta\rho g h_g + (P_w - P_{w0}) - p_e, \tag{15}$$

where $\Delta\rho = \rho_w - \rho_g$ is the density difference between brine and CO_2, h_g is the height of CO_2 which is obtained from the coarse-scale gas saturation S_g (after accounting for the reservoir rock-fluid characteristics), of the reservoir block connected to the fault block, P_w is the brine pressure in the reservoir, P_{w0} is the initial brine pressure in the reservoir, and p_e is the capillary entry pressure of the fault/fractures. The vertical gas leakage flux Q_{gf} along the fault is given as

$$Q_{gf} = \begin{cases} 0, & \psi \le 0 \\ \dfrac{A_f k_f}{\mu_g} \dfrac{(\psi + \Delta\rho g L_c)}{L_c}, & \psi > 0 \end{cases} \tag{16}$$

where A_f is the area of the fault perpendicular to flow, k_f is the vertical fault permeability and L_c is length of the caprock or the length of the fault connecting the reservoir to the secondary aquifer. This formulation accounts for the capillary entry pressure required for CO_2 to enter the fault. This approach relaxes the assumption of VE at the grid block where the fault is connected, allowing for non-zero vertical flow. However, for steady state single phase flow, fault leakage does not have a significant effect on reservoir predictions (Kang et al., 2014). By incorporating these key factors, the function aims to provide a more realistic representation of the fault leakage process.

2.3. Model Implementation

The leakage along the fault is numerically simulated as a fault leakage function, which is represented as a source/sink term in the material balance equations (Equation 10). This methodology circumvents the explicit discretization of faults, thereby capturing their impact on fluid flow and replicating their influence without requiring

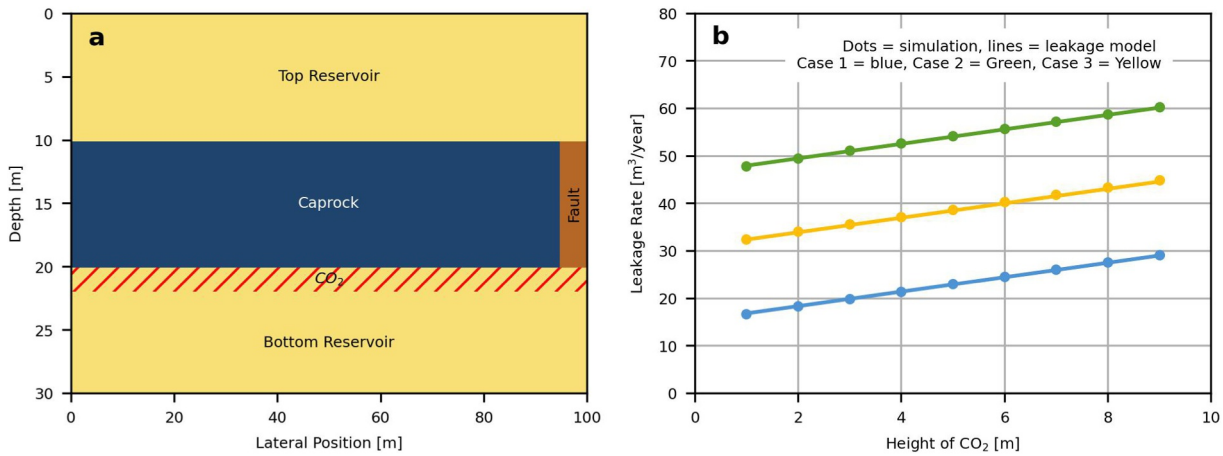

Figure 4. Grid representation of 2-D fine scale simulation (a) and fault leakage rate comparison between numerical simulation and VE model with fault leakage function (b). The three cases considered are: (1) hydrostatic reservoir and boundary pressure, (2) elevated reservoir boundary pressure, and (3) fault capillary entry pressure.

a computationally intensive, fully discretized fault representation. The fault leakage function is related implicitly to the primary unknowns of the reservoir model using the gas saturation and the overpressure terms of the grid blocks adjacent to the fault. The flow rate at the fault-reservoir interface is represented as shown in Equation 16. From a simulation perspective, fault leakage occurs when the leakage constraint, expressed as $\Delta\rho g h_g + (P_w - P_{w0})$, exceeds the fault capillary entry pressure p_e and the upscaled gas saturation is greater than zero. However, numerical experiments have demonstrated that this criterion can result in unstable behavior, characterized by frequent fluctuations (appearance and disappearance of the fault leakage term) during the iteration process and between time steps, which causes convergence issues and increased simulation time. To address this problem, the implementation of a smoothing function for the leakage rate term enables a more robust fault leakage function. We use a smoothing function, such that $\hat{Q}_{g\overline{f}} = Q_{\mathrm{gf}} f(\psi)$ with the smoothing function $f(\psi) = \left(1 - e^{(-\xi\,\psi)}\right)$ and the smoothing parameter ξ. In our simulations we use $\xi = 10^{-3}$ Pa^{-1} to regulate the fault leakage rate upon the initial occurrence of a non-zero fault leakage term. Under rigorous consideration, permitting the leakage constraint to marginally exceed p_e without initiating fault leakage introduces a minor inaccuracy in leakage rates. However, this approach has a negligible impact on long-term simulation results while significantly improving the efficiency of the simulations with respect to timesteps and convergence. The fault permeability assigned to the fault leakage term represents the vertical permeability of the damage zone only. The fault core is treated as impermeable, preventing across-fault flow, while the damage zone acts as the vertical conduit for CO_2 leakage to overlying formations. The resulting reservoir is discretized based on a finite volume discretization using the two-point flux approximation method, as implemented in the MRST (Lie, 2019) framework.

3. Results

In this section, we present the results obtained from applying the fault leakage function coupled with the VE reservoir model to several CO_2 injection scenarios.

3.1. Case 1—Comparison With 2D Simulations

The cases presented in this section are designed to verify our upscaled fault leakage function accurately reproduces the flow behavior of an explicitly gridded fault system. A 2D two-phase numerical model is used to simulate the fault leakage rates within the simplified CO_2 storage setting (Figure 4a). The objective of this case is to compare the fault leakage rates between the 2D numerical simulation with an explicit representation of the fault and the VE model with the fault leakage function proposed in this work. This case simulates fluid flow through a conceptual model comprising two horizontal aquifers separated by a caprock and connected by a vertical, conductive fault. The fault is treated as an equivalent porous medium with the reservoir, fault, fluid, and rock-fluid properties as specified in Table 1. Although the permeability of the aquifers and faults is simplified for

Table 1
Summary of Model Parameters Used for Fault Leakage Function Verification Simulation Described in Section 3.1

Property	Value
Bottom Reservoir and Top Reservoir Properties	
Top reservoir porosity	0.3
Bottom reservoir porosity	0.3
Top reservoir permeability (mD)	100
Bottom reservoir permeability (mD)	100
Reservoir overpressure (bars) (Case 2 and 3)	1
Caprock properties	
Caprock permeability (mD)	1×10^{-6}
Caprock porosity	0.05
Fault damage zone properties	
Fault damage zone porosity	0.03
Fault damage zone permeability (mD)	1
Fault damage zone width (m)	5
Fault damage zone length (m)	10
Fault damage zone capillary entry pressure (bars) (Case 3)	0.5
Bottom Reservoir, Fault and Top Reservoir Relative Permeability Properties	
Residual gas saturation	0
Residual brine saturation	0
Gas end-point relative permeability	1
Brine end-point relative permeability	1
Gas relative permeability exponent	1
Brine relative permeability exponent	1
Fluid properties	
Gas density (kgm^{-3})	500
Brine density (kgm^{-3})	1,000
Gas viscosity (Pa.s)	5×10^{-5}
Brine viscosity (Pa.s)	3.13×10^{-4}

comparative purposes, it is crucial to emphasize that the primary focus is on the interaction of these components, rather than precise geological representation.

A numerical grid of 12,000 cells discretizes the system with a resolution of 1 m x 1 m x .25 m (in the x, y, and z directions, respectively), resulting in a physical model with dimensions of 100 m × 30 m, consisting of three layers, each 10 m thick. The fault zone, located on the right side of the model, is 5 m wide and 10 m long. The system is assumed to be in hydrostatic equilibrium with 100% water saturation initially, and the relative permeability is governed by the Brooks-Corey model with parameters described in Table 1. No-flow boundaries are assumed at the top, bottom, and the right side (representing no flow across the fault core). The left boundary is treated as an open boundary, with the pressure maintained as hydrostatic. The system is initialized with a constant CO_2 column height at the left boundary of the storage reservoir. This column height and the boundary pressures can be varied to simulate buoyancy-driven and pressure-driven conditions, allowing for a comprehensive evaluation of the fault leakage modeling approach.

Three specific parametrizations are considered to compare the performance of the fault leakage modeling approach, (a) The reservoir and boundary pressures are hydrostatic. The pressure of the CO_2 column is derived solely from density differences, and the flow is driven by buoyancy. This parametrization mimics the migration phase of CO_2 storage. (b) The reservoir pressure is hydrostatic, but the boundary pressure is elevated to mimic the typical pressure increase observed during injection. The pressure of the CO_2 column is derived from both the density differences, and the pressure elevation. (c) Similar to Case 2, the third scenario contains an additional capillary entry pressure for the fault, which acts as a pressure barrier that the CO_2 must exceed to enter the fault zone. The 2D numerical simulations are run to steady-state conditions for each of the three cases. The leakage rate, specified as the flow leaving from the top of the fault, is then compared to the leakage rate obtained from the VE model with the fault leakage function (Figure 4b). The proposed fault leakage function shows excellent agreement with numerical simulations with explicitly gridded faults for all three scenarios. This demonstrates that it is suitable for capturing the same flow physics influencing fault-related CO_2 leakage, that is, buoyancy, pressure gradients, and capillary entry pressure. Moreover, the model's computational efficiency is improved by bypassing the explicit representation of the fault and top reservoir. This verification gives confidence that our model can be applied to field-scale CO_2 storage simulations.

It is important to highlight the potential limitations of the steady-state, single-phase fault leakage assumption used in our modeling approach. For instance, in the overpressure parametrization Equation 2 with a 5-m CO_2 column height, the calculated leakage rate is 53 m^3 per year. Accounting for the fault dimensions, this corresponds to a CO_2 Darcy flux of 0.03 m per day and the corresponding pore velocity of 1 m per day. This implies that it takes approximately 10 days, for the CO_2 to travel the 10-m distance separating the bottom reservoir and the top reservoir. Although faults are typically characterized by very low porosity, and the impact of CO_2 accumulation within the fault on the leakage rate may be minimal (Caine et al., 1996; Faulkner et al., 2010), there remains a delay in reaching the top reservoir that is not captured, because the current approach presupposes instantaneous leakage once the CO_2 reaches the base of the fault. This raises a pertinent question regarding the definition of leakage—whether it occurs once CO_2 enters the top reservoir or once it enters the fault from the bottom reservoir. However, the current modeling approach does not explicitly account for these dynamic effects during the fault leakage process. While acknowledging these limitations is crucial, it is equally important to contextualize the scale of typical CO_2 storage simulations, which extend from a few decades to a few centuries. Within this broader temporal framework, the steady-state, single-phase assumption may offer a reasonable approximation that allows

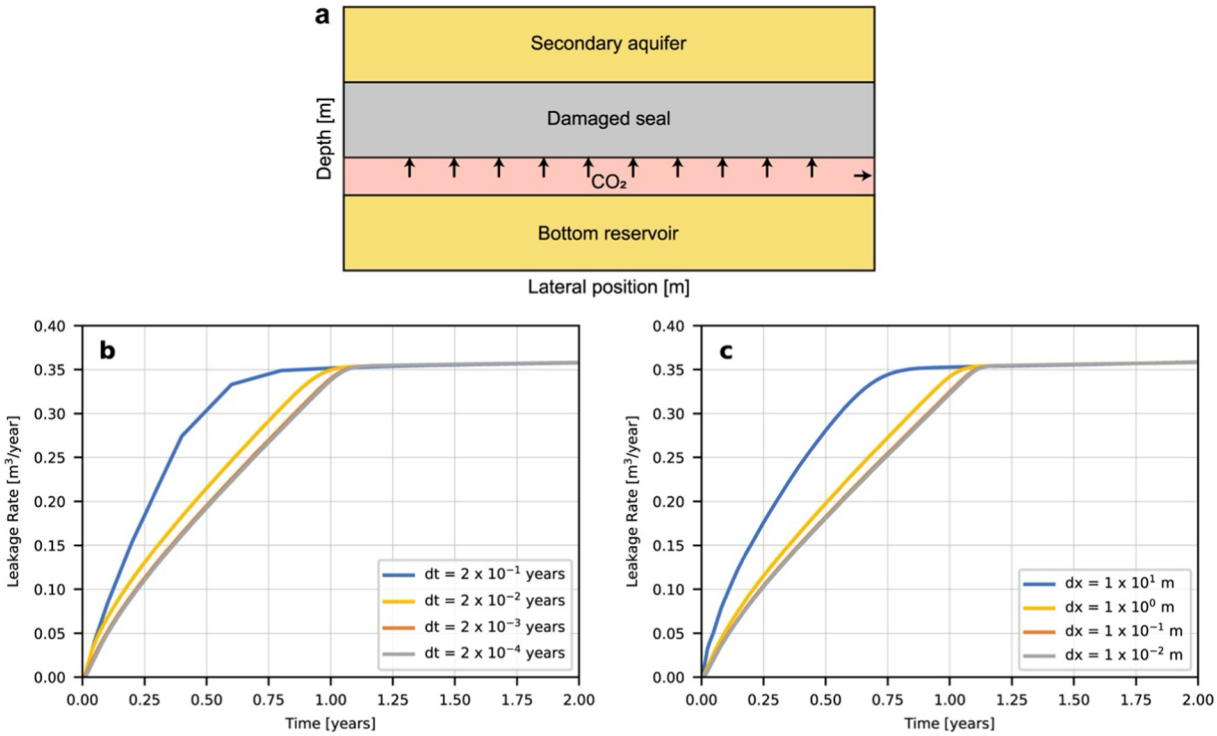

Figure 5. Conceptual representation of VE simulation setup of CO_2 storage with a damaged seal to assess the impact of grid block dimensions and time step size on leakage modeling (a), leakage rate comparison for varying time step sizes for a constant grid block dimension of 1 m (b) and leakage rate comparison for varying gridblock dimensions at a time step of 4×10^{-3} years (c).

us to screen leakage rates across a broad range of possible reservoir scenarios before commencing more detailed simulation studies that capture the full physics of fault leakage in a specific reservoir scenario. This consideration underscores the necessity of balancing model complexity with computational feasibility, particularly in the context of large-scale, long-term CO_2 storage simulations.

3.2. Case 2—Convergence Analysis

The following case aims to assess the impact of grid resolution and time step size on the fault leakage modeling methods presented in Section 2. A 2D, two-phase numerical model is employed to simulate leakage rates within a simplified CO_2 storage setting (Figure 5a). This case, with minor modifications, is based on the scenario described in Section 3.1. It simulates fluid flow through a geological model consisting of a horizontal aquifer located beneath a damaged seal, which behaves like a damage zone from the previous case. There is no fault core in this case. In this model, the caprock is replaced with a damaged seal, which is represented as a continuous leakage pathway, allowing any CO_2 accumulated beneath it to migrate upward and leak into a secondary aquifer. This seal extends horizontally across the reservoir and vertically into overlying strata, thereby hydraulically connecting the storage reservoir to a secondary aquifer. CO_2 leakage is quantified at the interface between the damaged seal and the secondary aquifer. To capture this vertical migration, the grid cells encompassing the damaged seal employ the fault leakage function and associated parameters specified in Table 2. The aquifer serves as the storage reservoir, and the damaged seal is treated as an equivalent porous medium. The properties of the reservoir, damaged seal, fluid, and rock-fluid interactions are specified in Table 2. For the purposes of testing numerical convergence and stability, we adopted simplified physical dimensions for both the aquifer and damaged seal (100 m wide and 10 m long). The objective of this case is to demonstrate that our implementation produces stable, converged solutions across different grid resolutions and time-step sizes. The system is assumed to be in hydrostatic equilibrium with an initial water saturation of 100%. Relative permeability is governed by the Brooks-Corey model, with parameters detailed in Table 2. No-flow boundaries are assumed at the top and bottom, while the left and right boundaries are treated as open, with pressure maintained as hydrostatic. The system is initialized with a constant CO_2 column height of 5 m at the left boundary of the storage reservoir. This column height and the

Table 2
Summary of Model Parameters Used for Convergence Analysis Simulation Described in Section 3.2

Property	Value
Reservoir Properties	
Reservoir porosity	0.3
Reservoir permeability (mD)	100
Damaged seal properties	
Damaged seal porosity	0.03
Damaged seal permeability (mD)	1×10^{-3}
Damaged seal length (m)	10
Reservoir and Damaged Seal Relative Permeability Properties	
Residual gas saturation	0
Residual brine saturation	0
Gas end-point relative permeability	1
Brine end-point relative permeability	1
Gas relative permeability exponent	1
Brine relative permeability exponent	1
Fluid properties	
Gas density (kgm^{-3})	500
Brine density (kgm^{-3})	1,000
Gas viscosity (Pa.s)	5×10^{-5}
Brine viscosity (Pa.s)	3.13×10^{-4}

boundary pressures can be varied to simulate buoyancy-driven and pressure-driven conditions, similar to those in Section 3.1. The grid blocks enclosing the damaged seal is modified to incorporate the fault leakage function, with properties mentioned in Table 2, to mimic along-fault leakage.

Figure 5b illustrates the leakage rate for 2 years with time steps varying from 2×10^{-1} years to 2×10^{-4} years and a grid block dimension of 1 m. Figure 5c illustrates the leakage rate for 2 years with grid block dimensions varying from 1×10^{1} m to 1×10^{-2} m and a time step of 4×10^{-3} years. A key observation is that the leakage rate converges toward a consistent solution for both, time and space. Coarser grids and larger time steps lead to overestimated leakage rates in the first year. Subsequently, all time steps and grid block sizes converge toward the same leakage rate predictions. While the total leakage increases with larger time steps and grid sizes, the magnitude of this increase becomes negligible after 100 years of simulation (when the system reaches steady state). For instance, the total leakage after 100 years is only 0.0025% higher for the 2×10^{-1} year time step compared to the 2×10^{-3} year time step, and 0.0027% higher for the 1×10^{1} m grid size compared to the 1×10^{-2} m grid size. Resizing grid blocks proportionally resizes the fault leakage function, ensuring the total damaged seal width remains constant. Consequently, the number of leakage terms increases with a higher number of grid blocks. Despite this increase, the impact on total leakage predictions remains relatively low. It is important to acknowledge that this model uses a fault leakage function instead of explicitly representing the faults, to ensure computational efficiency. Despite this simplification, the model is able to approximate the reservoir behavior and leakage rates outcomes with sufficient reliability. This approach facilitates the rapid screening of potential storage sites, enabling the identification of promising candidates. Consequently, resources can be strategically allocated to design comprehensive data acquisition campaigns tailored to the specific geological complexities of selected sites. By expediting the early screening phase, this methodology contributes to the overall acceleration of CO_2 storage project development in geologically complex settings.

3.3. Case 3—Sloping Reservoir With a Leaky Fault

The case presented in this section is designed to test the fault leakage function for a gently sloping reservoir with a large fault. The conceptual model comprising a gently sloping reservoir connected to a secondary aquifer by a fault is shown in Figure 6. The reservoir is discretized as a VE grid with 2,500 cells, each measuring 20 m × 20 m in the *x* and *y* directions, respectively, resulting in a physical model with dimensions of 1,000 m × 1,000 m. The reservoir has a thickness of 10 m and a slope of ∼3°. The fault is treated as an equivalent porous medium using the

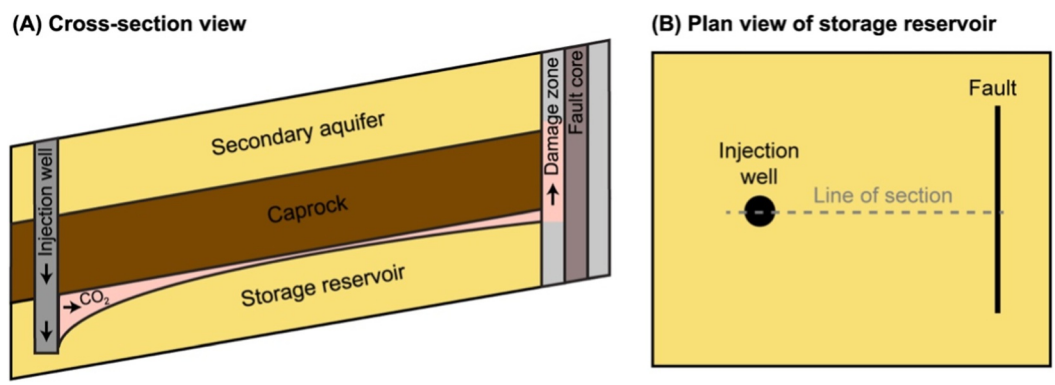

Figure 6. The conceptual model showing a gently sloping reservoir connected to a secondary aquifer by a leaky fault in the cross-section view (a) and the reservoir in plan view (b).

Table 3
Summary of Model Parameters Used for the Sloping Reservoir Simulation Case Described in Section 3.3

Property	Value
Reservoir description	
Number of cells (NX*NY)	50 × 50
Cell dimensions (DX*DY) (m)	20 × 20
Reservoir height (H) (m)	10
Reservoir slope (degrees)	2.86
Average reservoir depth (m)	975
Porosity	0.3
Permeability (mD)	100
Rock compressibility (Pa^{-1})	4.35×10^{-10}
Fluid properties (at 2,000 m depth)	
Brine viscosity (Pa.s)	3.13×10^{-4}
Gas viscosity (Pa.s)	3.21×10^{-5}
Brine density (kgm^{-3})	1,001
Gas density (kgm^{-3})	389.7
Fault damage zone properties	
Fault damage zone permeability (mD)	1×10^{-3}
Fault damage zone width (m)	5
Fault damage zone length (m)	100
Rock-Fluid properties	
Residual gas saturation	0.2
Irreducible brine saturation	0.27

fault function, and the reservoir, fault, fluid, and rock-fluid properties as specified in Table 3. The fault is positioned to intersect the reservoir and extend vertically into the caprock and hydraulically connect the storage reservoir to a secondary aquifer. Leakage is measured at the top of the fault (fault-secondary aquifer interface), capturing the rate of CO_2 exiting the storage reservoir along the fault. The grid blocks enclosing the fault are modified to (a) set the across-fault permeability within the reservoir to zero, mimicking an impermeable fault core, and (b) incorporate the fault leakage function with the properties mentioned in Table 3 to mimic along fault leakage. The system is assumed to be in hydrostatic equilibrium with 100% water saturation initially, and the relative permeability is governed by the Brooks-Corey model with parameters mentioned in Table 3. No-flow boundaries are assumed at the top, right and left boundaries of the VE reservoir. The bottom boundary is treated as an open boundary with the pressure maintained as hydrostatic. Hence this bottom boundary acts as a sink for the heavier brine phase and allows for up-dip movement of CO_2. Unlike previous simulations where the CO_2 injection was controlled by boundary conditions, this simulation uses the rate constrained well for CO_2 injection. The injection location is at the coordinate pair (100, 500 m) for an injection rate of 1,229 tons per year over 3 years followed by 97 years of migration. The fault zone is located in the center of the model., that is, 500 m away from either side boundary in *x*-direction as shown in Figure 7a. The fault is 800 m long in the *y*-direction. The goal of this case study is to analyze the evolution of CO_2 leakage rates and assess the impact of fault capillary entry pressure on these rates.

VE reservoir simulation is conducted with a time step of 1 year to evaluate the impact of the fault on the migration of a CO_2 plume within the reservoir. The evolution of the CO_2 plume is depicted at the end of the injection period (Figure 7b) and after 97 years of migration (Figure 7c). The simulation results demonstrate the preferential up-dip movement of the CO_2 plume within the reservoir. Notably, significant quantities of CO_2 are observed to accumulate at the base of the fault since the impermeable fault core inhibited further across-fault migration within the reservoir. This leads to an increase in gas saturation down dip of the fault until the CO_2 plume migrated laterally to the fault tips, after which it continued its unhindered up-dip movement. Leakage along the fault occurs once the CO_2 reached the fault. The leakage rate reached its maximum and then reduced after the CO_2 migrated around the fault tips. After this point, continued upward migration reduced the amount of CO_2 trapped below the fault, consequently decreasing the leakage rates (Figure 7d). This case demonstrates the tool's capability to capture several key aspects of fault-reservoir interaction. First, CO_2 accumulation at the fault barrier and subsequent lateral migration around fault tips reflects realistic plume behavior in faulted systems. Second, the temporal evolution of leakage rates, increasing as CO_2 accumulates, then decreasing as the plume migrates past the fault, illustrates dynamic coupling between reservoir flow and fault leakage.

The introduction of a capillary entry pressure constraint for fault leakage reveals interesting leakage dynamics. Figure 7d depicts the leakage rates, while Figure 7e shows the cumulative leakage after 100 years for varying fault capillary entry pressures ranging from 0 to 0.1 bar. Both the maximum fault leakage rate and cumulative leakage decrease with the increase in fault capillary entry pressure. The scenario with zero fault capillary entry pressure represents unconstrained leakage along the fault, allowing for continuous CO_2 leakage. In contrast, higher capillary entry pressures act as a barrier, limiting the extent of CO_2 migration and leakage through the fault zone. An important observation pertains to the leakage rate reaching zero. This occurs when the trapped CO_2 plume is unable to overcome the capillary entry pressure barrier, effectively stopping further leakage along the fault. The time at which leakage ceases decreases with the increase in fault capillary entry pressure, highlighting its potential for mitigating leakage.

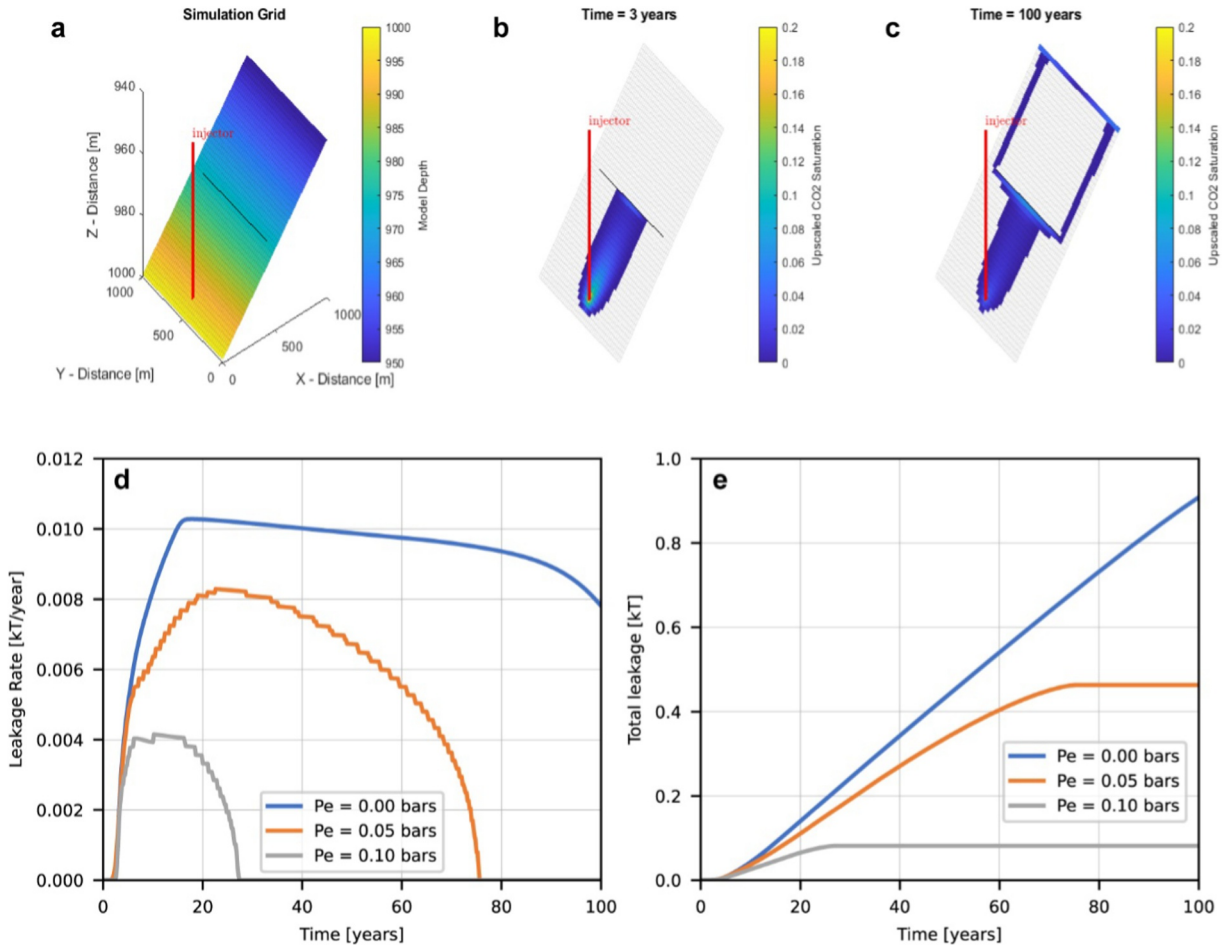

Figure 7. Simulation of CO_2 plume migration in a sloping reservoir (note vertical exaggeration) and leakage along a fault showing the inclined 3D-view of the reservoir and the location of the fault (a), the CO_2 plume saturation distribution at the end of the injection period (b) the CO_2 plume saturation distribution after 100 years of migration (c), the CO_2 leakage rates along the fault for different fault capillary entry pressures (d) and the cumulative CO_2 leakage after 100 years for different fault capillary entry pressures (e).

3.4. Case 4—Field-Scale Fault Leakage Quantification

The *J* area, a conceptual CO_2 storage site within the Malay Basin offshore Peninsular Malaysia, is used to illustrate the fault leakage function coupled with VE models for field-scale fault leakage quantification. The Malay Basin is approximately 500 km long, 200 km wide, and 12 km deep, situated in coastal waters less than 100 km from the east coast of Peninsular Malaysia (de Jonge-Anderson et al., 2024b). It is a mature hydrocarbon basin with over 181 discoveries and over 14.8 billion barrels of oil equivalent in recoverable resources discovered since 1981 (Madon, 2021). Recently, it has been considered an important area for CCS (Abd Rahman et al., 2022; Hasbollah et al., 2020) due to its numerous mature fields that could be repurposed, providing an abundance of data and production history. Saline aquifers offer great additional potential, however, limited data and understanding necessitate uncertainty assessment and screening analysis to determine storage traps.

The *J* area lies on the northern margin of the basin, 50 km from the nearest hydrocarbon field with the target reservoir situated at 1,984 m depth below the seafloor. The main storage interval consists of a thick and heterogeneous sequence of lower to middle Miocene sandstones, mudstones, and coals, with the sandstones representing the target reservoir. The 3D reservoir grid, depths, petrophysical and reservoir properties are obtained from de Jonge-Anderson et al. (2024a, 2024b). These studies focused on storage capacity assessment without considering faults or leakage. Here we build on these studies and their well-characterized field-scale grid to demonstrate the applicability of the fault leakage function developed in this study. The relevant reservoir properties are summarized in Table 4. Previous storage capacity assessment for this site have identified the best

Table 4
Summary of Model Parameters Used for Field-Scale Fault Leakage Quantification Simulation Case Described in Section 3.4 (Adapted From (de Jonge-Anderson et al., 2024b))

Property	Value
Reservoir description	
Number of cells (NX*NY*NZ)	100 × 110 x 5
Cell dimensions (DX*DY) (m)	200 × 200
Area (km^2)	440 (22 × 20)
Average top reservoir depth (m)	1,984
Porosity	0.05–0.25 (arithmetic mean = 0.145)
Permeability (mD)	1.2–241 (arithmetic mean = 39.4)
Rock compressibility (Pa^{-1})	4.35×10^{-10}
Seafloor temperature (°C)	24
Temperature gradient (°Ckm^{-1})	50
Seafloor Depth (m)	70
Fluid properties (at 2,000 m depth)	
Brine viscosity (Pa.s)	3.13×10^{-4}
Gas viscosity (Pa.s)	3.21×10^{-5}
Brine density (kgm^{-3})	1,001
Gas density (kgm^{-3})	389.7
Fault damage zone properties	
Fault damage zone permeability (mD)	1×10^{-3}
Fault damage zone width (m)	5
Fault damage zone length (m)	500
Rock-Fluid properties (Brooks-Corey Model)	
Residual gas saturation	0.2
Irreducible brine saturation	0.27
Gas end-point relative permeability	1
Brine end-point relative permeability	1
Gas relative permeability exponent	1
Brine relative permeability exponent	1

injection location at the coordinate pair (413,100, 718,500 m) (UTM 48 N – reference coordinate system) for an injection rate of 1 Mt per year over 30 years followed by 970 years of migration (de Jonge-Anderson et al., 2024b). The top of the reservoir lies at depths between 1,500 and 2,500 m below a seafloor depth of 70 m. The reservoir pressure is assumed hydrostatic with a temperature profile following a geothermal gradient of 50°C/km and a seafloor temperature of 24°C (Madon & Jong, 2021).

The conceptual model comprising the storage reservoir connected to a secondary aquifer by a fault is shown in Figure 8. A 26 km-long fault is introduced into this grid as shown in Figure 9a and the fault properties are provided in Table 4. The fault introduced here is synthetic and designed specifically to evaluate the leakage modeling capabilities of the proposed methodology. Information was not available on actual fault properties in the *J* area, and characterization of real faults would be required for site-specific risk assessment. For the purposes of demonstrating our tool's field-scale applicability, the synthetic fault serves to illustrate how the method can be applied to realistic reservoir geometries and evaluate sensitivity to uncertain fault parameters. The synthetic fault is positioned to intersect the reservoir and extend vertically into the caprock and hydraulically connect the storage reservoir to a secondary aquifer. The grid blocks surrounding the fault are adjusted: (a) assign zero transmissibility across the fault within the storage reservoir, representing an impermeable fault core, and (b) insert the fault leakage function to mimic along fault leakage to secondary aquifer, utilizing the properties listed in Table 4.

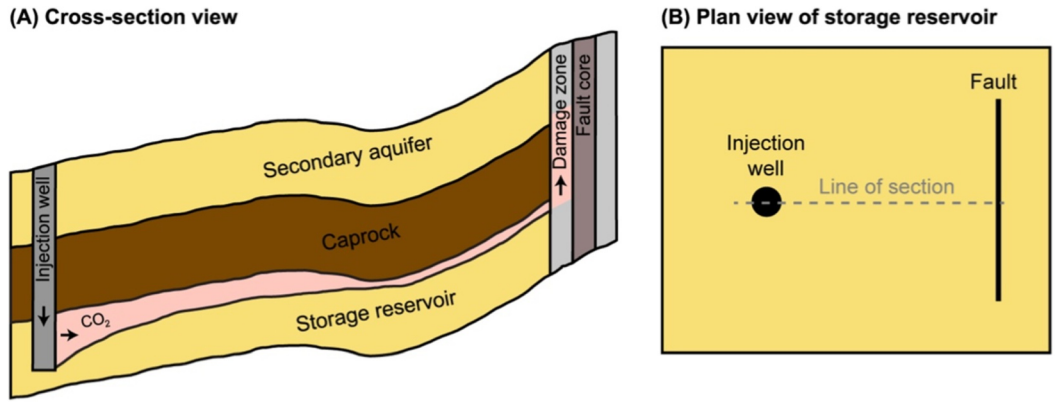

Figure 8. The conceptual model of storage reservoir connected to a secondary aquifer by a leaky fault is shown in cross-section view (a) and the storage reservoir is shown in plan view (b).

Leakage is measured at the top of the fault (fault-secondary aquifer interface), capturing the rate of CO_2 exiting the reservoir along the fault. The injection well is located 12 km away from the fault. The model boundaries are treated as open, with the pressure maintained at hydrostatic conditions. The goal of this case study is to understand the impact of fault leakage on the injection rate and storage capacity within the *J* area.

A numerical simulation is performed to assess the impact of a fault on the migration and leakage of a CO_2 injected into the reservoir (Figure 9a). The evolution of the CO_2 plume is depicted at the end of the injection period

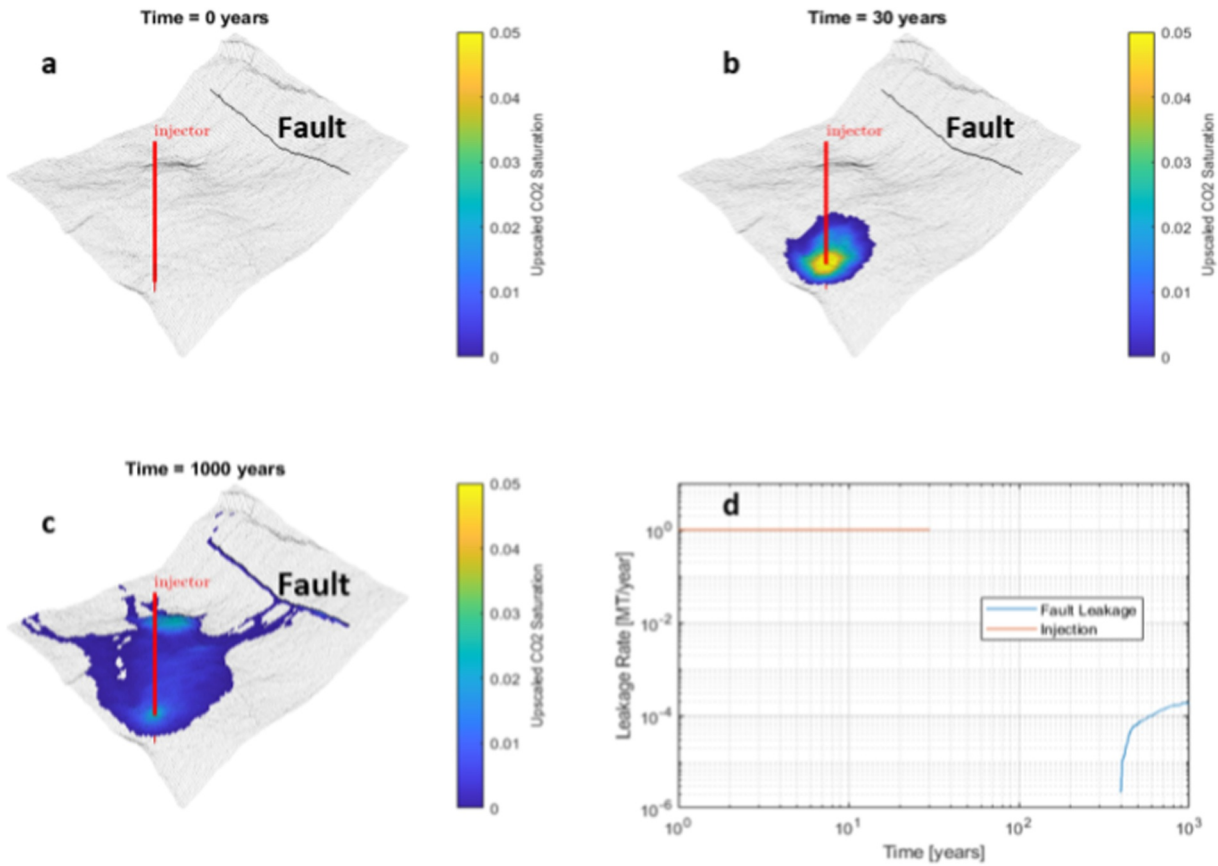

Figure 9. Simulation of CO_2 plume migration and leakage along a leaky fault. Inclined 3D view of the reservoir showing the location of the fault (a), CO_2 plume saturation distribution at the end of the injection period (b), CO_2 plume saturation distribution after 1,000 years of migration (c) and temporal evolution of the CO_2 leakage rate along the fault (d).

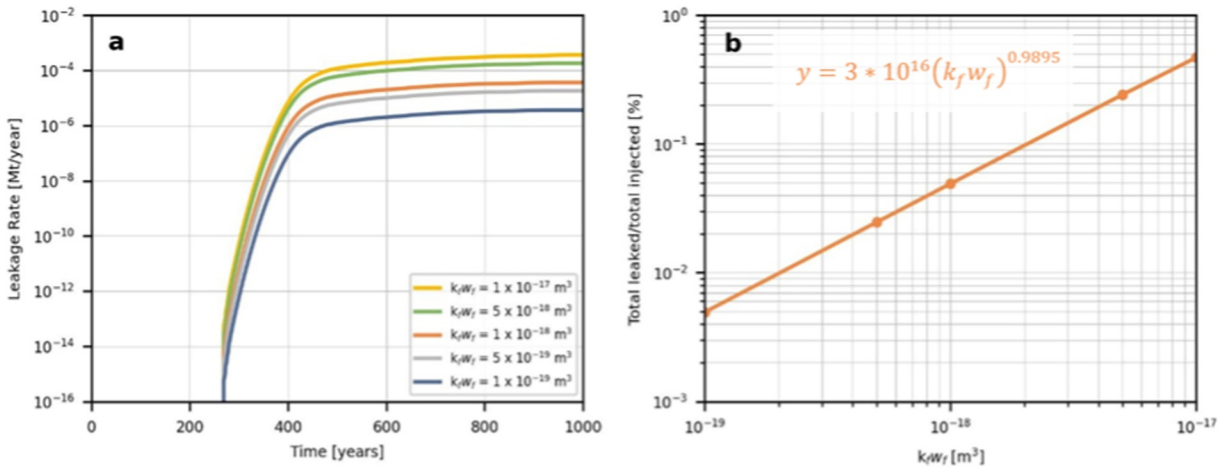

Figure 10. Impact of fault properties on CO_2 leakage showing the relationship between fault permeability, damage zone thickness, and the magnitude of CO_2 leakage (a) and the decrease in total CO_2 leakage over time with decreasing value for the product of fault permeability and damage zone thickness $k_f w_f$ (b).

(Figure 9b) and after 1,000 years of the migration phase (Figure 9c). The simulation results show the CO_2 plume moving up-dip and accumulating within an anticline structure. Considerable amounts of CO_2 accumulate at the base of the fault, with the impermeable fault core preventing further migration across the fault. The CO_2 plume reaches the fault after approximately 400 years and immediately begins leaking through the fault (Figure 9d). The leakage rate increases as more of the migrating CO_2 became trapped at the faulted block representing the hanging wall. By the end of the 1,000-year simulation period, a total of 30 Mt of CO_2 has been injected, of which 0.085 Mt (0.28%) has leaked along the fault. These results highlight the impact that the presence of a fault can have on the migration and containment of a CO_2 plume in a storage setting and the ability to address this impact quickly as each simulation takes under 30 s on Apple MacBook Pro with the Apple M1 chip.

The fault permeability and the thickness of the damage zone play a crucial role in determining the magnitude of CO_2 leakage, as shown in Figure 8. While these parameters do not affect the onset of leakage (Figure 10a). The total amount of leakage decreases, following a power-law trend with an exponent of 0.9895 as the product of fault permeability and damage zone thickness $k_f w_f$ decreases (Figure 10b). While Equation 16 predicted an exponent of 1, the observed deviation suggests that variations in pressure buildup induced by fault permeability also influence leakage rates. These effects are captured within the presented function. The fault permeability is strongly dependent on the thickness of the damage zone, as well as the inter-connectedness and density of the fracture networks within the damage zone, and studies have demonstrated that these fault zone parameters are influenced by the pressure within the reservoir-caprock-fault system (Rutqvist, 2012; Vilarrasa et al., 2017).

The fault damage zone capillary entry pressure represents the minimum differential pressure required for CO_2 to overcome and enter the fault damage zone, controlled by the effective aperture of the largest pore throats or fracture openings (Espinoza & Santamarina, 2017; Manzocchi et al., 2010; Zheng and Espinoza, 2022). The physics of leakage governed by capillary entry pressure has been demonstrated through theoretical and experimental studies showing that flow occurs where fluid pressure exceeds this threshold (Sayag and Neufeld, 2016). Importantly, as shown in Equation 15, the driving potential for fault leakage depends on the combined effects of buoyancy from CO_2 accumulation, injection-induced reservoir overpressure, and the resisting capillary entry pressure. This coupling means that fault leakage behavior depends on both geological properties (entry pressure, permeability), fluid properties (buoyancy) and operational decisions (injection rate and pressure, total injected volume, well placement). The ability to rapidly evaluate these trade-offs between geological uncertainty and operational constraints is essential during site screening when multiple candidates and injection strategies must be assessed.

We demonstrate this capability by varying fault capillary entry pressures (Figure 11) in the preceding simulation for the *J* area. As the entry pressure increases from 0 to 0.75 bar, leakage onset is progressively delayed, and maximum leakage rates decrease due to the reduced driving potential. For this specific injection scenario (1 Mt/year for 30 years) and reservoir configuration, an entry pressure of 1.0 bar prevents any leakage over the 1,000-

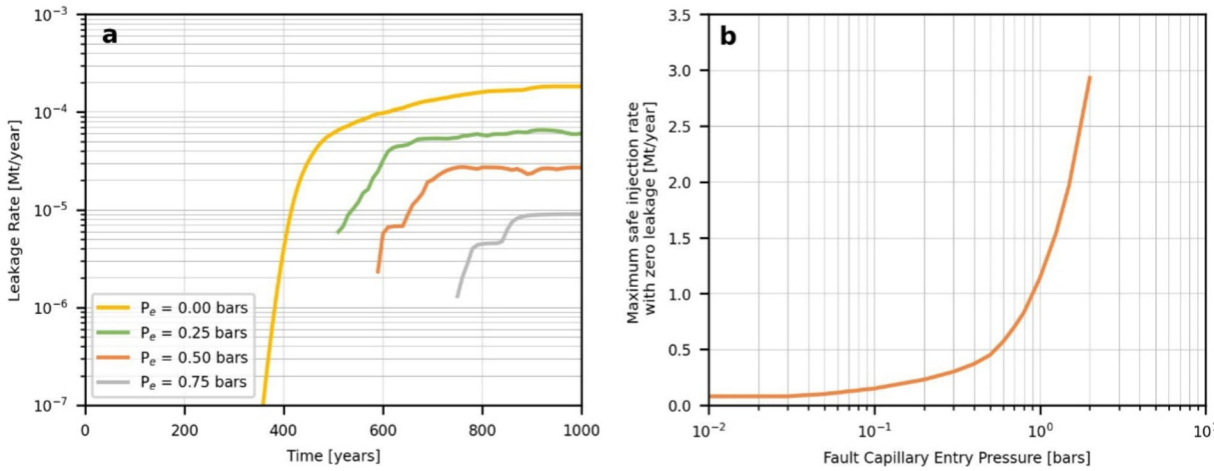

Figure 11. Impact of fault capillary entry pressure on CO_2 leakage showing the leakage profile for different fault capillary entry pressures where higher entry pressures act as a barrier, delaying and reducing the CO_2 leakage and no leakage occurs for a scenario of 1 bar (a). Maximum injection rate with zero leakage for a range of fault capillary entry pressures where increasing the entry pressure allows for higher injection rates without CO_2 leakage (b).

year simulation period. Figure 11b shows that higher entry pressures permit higher injection rates before leakage occurs. The observation that a 1 bar entry pressure prevents leakage in this scenario reflects the specific pressure evolution and CO_2 accumulation pattern resulting from the reservoir-injection configuration. With injection 12 km from the fault, pressure diffusion over this distance limits overpressure at the fault location, while the buoyancy-driven accumulation produces a CO_2 column insufficient to generate the equivalent 17-m height needed to overcome the 1 bar threshold. The combined driving potential (buoyancy plus overpressure) never exceeds the capillary barrier. A different configuration, for instance, injection closer to the fault or a structural setting promoting greater CO_2 accumulation at the fault base could generate higher driving potentials, making the same 1 bar entry pressure insufficient to prevent leakage. This sensitivity highlights that fault sealing capacity cannot be assessed from entry pressure alone; it depends critically on the interplay between reservoir-scale pressure propagation, CO_2 migration patterns, and fault properties.

Our earlier analysis assumed zero across-fault flow (transmissibility multiplier, $\gamma_T = 0$), representing a worst-case scenario where the low-permeability fault core acts as a complete barrier within the reservoir. In reservoir simulation, transmissibility multipliers quantify the hydraulic conductivity across faults, scaling the flow between adjacent grid cells from 0 (complete sealing) to 1 (no flow impedance). These multipliers depend on fault zone properties including fault core thickness and permeability relative to the reservoir rock (Manzocchi et al., 1999). To assess the sensitivity of leakage predictions to this assumption, we conducted simulations with tm values ranging from 0 to 1.0, maintaining zero fault capillary entry pressure and all other parameters from Table 4. This analysis considers only across fault transmissibility; capillary barriers within the fault core are not included.

Figure 12 shows that cumulative leakage decreases substantially as across-fault flow increases. The zero-flow assumption ($\gamma_T = 0$) yields maximum leakage with a case having essentially impermeable fault ($\gamma_T = 10^{-3}$) producing nearly identical results. This verifies our conservative assumption that highly sealing faults behave similarly to completely sealed faults. However, as transmissibility multiplier increases beyond 10^{-3}, leakage rates decline progressively, with $\gamma_T = 0.1$ reducing total leakage by approximately 55% and $\gamma_T = 1$ (fully permeable fault core) reducing it by 87% relative to the sealed case. When the fault core allows flow, migrating CO_2 can pass through the fault within the reservoir. This reduces the plume height of CO_2 along the fault base, decreasing the driving potential for vertical leakage. These results demonstrate that the zero across-fault flow assumption provides an upper bound on leakage estimates, appropriate for conservative early stage screening when fault core properties are uncertain.

4. Discussion

One of the key strengths of the proposed approach is its computational efficiency. By employing the VE approximation instead of 3D grids and detailed multiphase flow simulations, the model significantly reduces

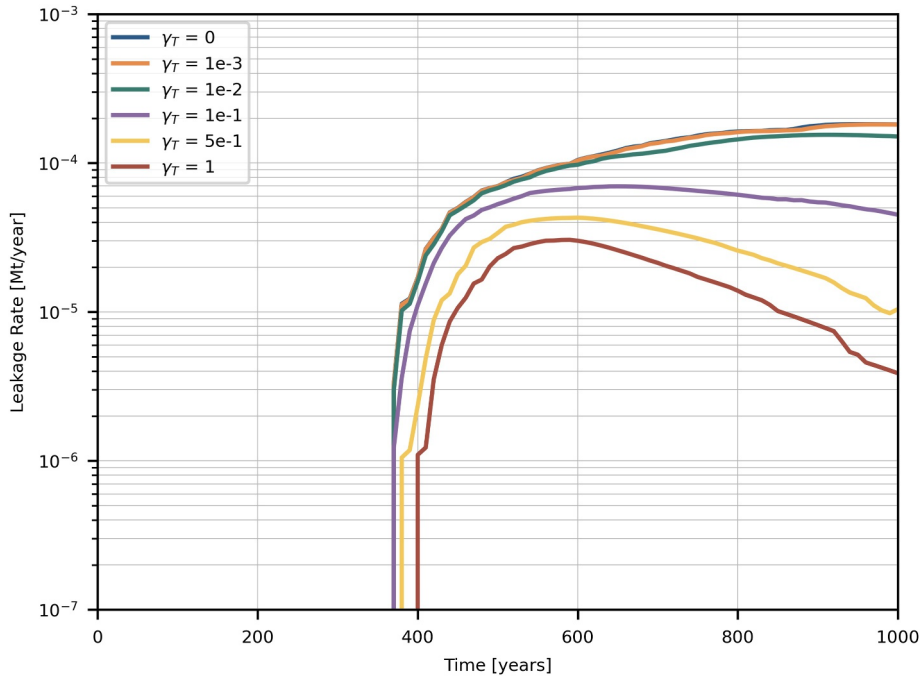

Figure 12. Sensitivity of leakage rates to transmissibility multiplier (γ_T). Six cases are shown ranging from completely sealed ($\gamma_T = 0$) to fully permeable ($\gamma_T = 1$) fault cores. Total cumulative leakage over 1,000 years is shown in the legend.

processing time and resources (Nilsen et al., 2016a, 2016b; Nordbotten & Celia, 2011). For example, in the Malay Basin case study (Section 3.4), it produced predictive results for a 440 km^2 area with a leaky fault in under 30 s. This speed is particularly valuable for early stage CCS project development, where multiple candidate sites must be rapidly screened (Pawar et al., 2015). In addition, the simplicity of the analytical fault leakage function enables straightforward integration into established VE simulation workflows, promoting wider adoption, especially for projects limited by sparse data or computational resources (Andersen, 2017).

The four simulation cases highlight the model's versatility in assessing along-fault leakage under varying conditions. Case 1 demonstrated strong agreement between VE-fault leakage function results and 2D numerical simulations with explicitly gridded faults, confirming the analytical fault leakage function's accuracy. Case 2 revealed the model's robustness under varying grid resolutions and time step sizes; although coarser grids and larger time steps initially overestimated leakage rates, the results converged at steady state, ensuring stability across different computational setups. In Case 3, introducing fault capillary entry pressure in a sloping reservoir scenario revealed its critical influence on leakage control: higher entry pressures delayed leakage onset and reduced cumulative leakage, underscoring the importance of this parameter in CCS design. Finally, Case 4 applied the model to the field-scale Malay Basin, showing leakage sensitivity for wide range of certain parameters and demonstrating its practical applicability in realistic geological settings. Our assumption of zero across-fault flow within the reservoir represents a conservative worst-case scenario. In reality, fault cores often have finite permeability allowing some across-fault flow (Ketterman et al., 2020; Manzocchi et al., 2010; Pei et al., 2015; Yielding et al., 2010), which would reduce CO_2 accumulation at the fault base and decrease vertical leakage. Section 3.4 demonstrates how incorporating across-fault flow through transmissibility multipliers affects leakage predictions.

Collectively, these cases deepen our understanding of how fault properties impact leakage behavior. Increased fault permeability, particularly under pressure-driven conditions, can substantially elevate leakage rates, emphasizing the need for detailed permeability characterization during site selection (Bjørnarå et al., 2023; Rizzo et al., 2024; Salo-Salgado et al., 2023). The capillary entry pressure analysis illustrated the interaction between operational conditions (injection rate and pressure, pressure buildup) and geological properties (capillary entry pressure) in controlling leakage onset and magnitude. Higher capillary entry pressure delayed leakage onset and reduced cumulative leakage, demonstrating how this parameter constrains the driving potential for fault leakage

(Equation 15). Beyond these individual insights, the model's ability to rapidly evaluate fault leakage risks enables strategic decision-making in geologically complex settings. By identifying sites with lower containment risks early on, the model helps allocate computational resources more efficiently. On the other hand, if gigatonne-scale storage is to be achieved in the coming decades (Krevor et al., 2023), it is imperative to move beyond the simpler "Class A" storage sites (Ringrose & Meckel, 2019). These could include sites with a degree of fault-related leakage risk and this model's scalability, and speed could prove crucial to rapidly evaluating and de-risking such areas.

An inherent challenge in fault modeling is the uncertainty associated with fault property data. Although it is helpful that the proposed model captured the sensitivity of fault permeability and fault capillary entry pressure on total leakage, obtaining more detailed data on fault geometry, stress regimes, and fracture networks could improve the accuracy of leakage predictions (Rizzo et al., 2024; Snippe et al., 2022). The assumption of constant fault permeability and capillary entry pressure may not adequately capture the heterogeneity present in real-world faults. Future studies should explore the impact of spatial variability in fault properties using stochastic modeling techniques (Berge et al., 2022; Bjørnarå et al., 2023; Salo-Salgado et al., 2023). The model assumes pre-existing fault permeability and does not account for stress-induced permeability changes, fault reactivation, or pressure-stress coupling. These geomechanical processes can significantly alter leakage behavior, particularly over decadal to centennial timescales, and have been demonstrated to control leakage onset, duration, and magnitude (Castelletto et al., 2013; Chang & Segall, 2016; Chen et al., 2024; Jha & Juanes, 2014; Meguerdijian and Jha, 2021; Rinaldi et al., 2014; Rutqvist, 2012; Vilarrasa et al., 2017; Zhao and Jha, 2019). Fault reactivation and fracture opening can increase damage zone permeability by a few orders of magnitude, though the magnitude of change varies significantly with fault architecture and stress conditions (Aben et al., 2020; Mitchell & Faulkner, 2012; Petrie et al., 2014; Rizzo et al., 2024; Simpson et al., 2001). In particular, if a fault is critically stressed, injection pressures sufficient for storage operations could induce reactivation and elevate permeability beyond the range considered during screening, potentially causing the model to underestimate leakage risk and misclassify a site as suitable for storage. Moreover, positive feedback mechanisms, such as fault slip triggering further fracture opening which accelerates permeability increase are not represented here. Nevertheless, the sensitivity analyses presented in Case 4 evaluate leakage across fault permeability ranges that encompass values produced by activation, allowing potential risks to be bounded without explicitly modeling the underlying mechanisms. The computational efficiency of the proposed approach makes such wide-range parameter exploration tractable at the screening stage. In fields containing multiple faults, this capability allows the identification of faults that pose the greatest leakage risk, thereby focusing data acquisition efforts and subsequent coupled geomechanical simulations. While the model has been verified against synthetic scenarios and benchmark simulations, further validation using real-world data sets would strengthen its applicability and reliability (Choi et al., 2023; Michie et al., 2021).

5. Conclusions

This work presents a fast and computationally efficient tool for simulating fault leakage under uncertainty for realistic, field-scale CO_2 storage applications. Faults are inherently complex, typically characterized by a fault core and a surrounding fractured damage zone, both of which significantly influence fault leakage behavior at the field scale. Explicitly representing these fault complexities along with the multi-layered systems is a computationally intensive method for resolving fault leakage-related uncertainty, especially during the early stages of storage site screening when data availability is limited. The primary contribution of this work addresses this challenge by proposing an approach that integrates an upscaled fault leakage function, specifically tailored to the unique characteristics of the fault core, damage zone, and flow properties, into a VE reservoir modeling framework. The proposed tool is a cost-effective method for early stage screening of fault leakage risk during CO_2 storage site selection. By enabling rapid evaluation of multiple sites and uncertainty scenarios, it allows identification of potential suitable candidates warranting detailed investigation. Sites identified through this screening process should subsequently undergo rigorous coupled thermal-geomechanical-dynamic modeling for detailed characterization, with the screening results directly informing which faults require detailed geomechanical characterization and which parameters dominate leakage risk. This two-stage workflow allows strategic allocation of computational and data acquisition resources to sites with greatest storage potential. The tool's computational efficiency, demonstrated by 30-s runtimes for the Malay Basin case study, enables the extensive uncertainty quantification necessary during early project stages when subsurface data is limited. Such fast

screening of potential storage sites is key to enabling the scale-up of CO_2 storage and achieving the gigaton-scale deployment needed to reduce global CO_2 emissions.

The findings from the simulation cases provide valuable insights into the roles of fault permeability and capillary entry pressure in controlling CO_2 leakage rates. The results highlight the importance of accurately characterizing these fault properties and incorporating capillary entry pressure constraints into CCS site assessments. The ability of the proposed model to handle a range of scenarios, from synthetic benchmarks to field-scale applications, demonstrates its versatility and practical relevance to CO_2 storage characterization studies. The current assumptions of steady-state leakage and constant fault properties limit the ability to capture dynamic behaviours such as fault reactivation or pressure changes over time. Future studies should address these limitations by incorporating geomechanical processes and stochastic variability in fault properties. Additionally, testing the model against diverse field data sets will enhance confidence in its broader applicability and reliability.

Appendix A: Sensitivity to Smoothing Parameter

The smoothing parameter ξ in the fault leakage function (Section 2.3, Equation 16) regulates the transition when the driving potential ψ approaches the capillary entry pressure threshold and the initial occurrence of a non-zero fault leakage term. To assess whether simulation results are sensitive to this parameter, we conducted an analysis using the simulation setup from Case 4 (Section 3.4) with zero capillary entry pressure and parameters specified in Table 4. Figure A1 shows the temporal evolution of fault leakage rates for three different smoothing parameter values ($\xi = 10^{-4}$, 10^{-3}, and 10^{-2} Pa^{-1}) alongside a case with no smoothing ($f(\psi) = 1$, i.e. $\xi \to \infty$). All four curves are nearly identical, except for $\xi = 10^{-4}$ Pa^{-1} where it underpredicted leakage, demonstrating that the smoothing parameter has minimal impact on leakage magnitudes for $\xi > 10^{-3}$ Pa^{-1}. This is because the smoothing function primarily affects behavior when ψ is within a few pascals of the threshold. For typical CO_2 storage conditions, where driving potentials significantly exceed this narrow transition zone, the smoothing has negligible impact on predicted leakage rates. The value $\xi = 10^{-3}$ Pa^{-1} used throughout this study provides numerical stability without meaningfully altering results.

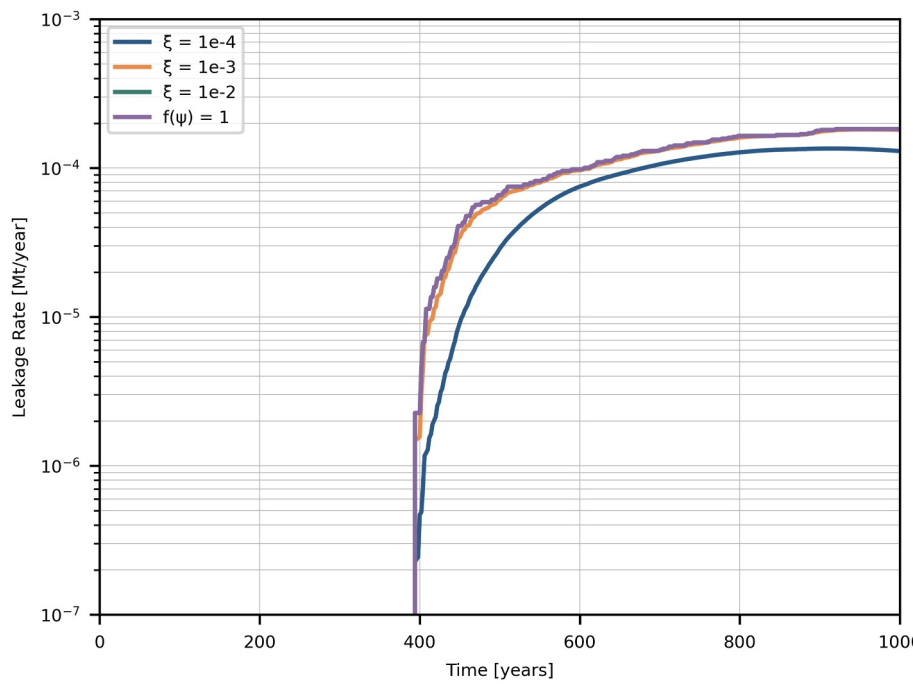

Figure A1. Sensitivity of fault leakage rates to the smoothing parameter ξ for the Malay Basin case with zero fault capillary entry pressure. Four cases are shown: $\xi = 10^{-4}$ Pa^{-1} (blue), $\xi = 10^{-3}$ Pa^{-1} (orange), $\xi = 10^{-2}$ Pa^{-1} (green), and no smoothing with $f(\psi) = 1$ (light blue).

Conflict of Interest

The authors declare no conflicts of interest relevant to this study.

Availability Statement

Simulations were conducted using the CO_2-lab module of the open-source MATLAB® Reservoir Simulation Toolbox, MRST, available at https://www.sintef.no/projectweb/mrst/. The fault leakage function module is on GitHub (https://github.com/Poriyalar/faultve) and available at zenodo (Ramachandran, 2025).

Acknowledgments
The funding and data underpinning this work was provided by PETRONAS via the (PACESET), based at Heriot-Watt University. Sebastian Geiger thanks Energi Simulation for supporting his Chair in Sustainable Geoenergy. Florian Doster acknowledge valuable discussions with Michael A. Celia, Jan M. Nordbotten and Mary Kang while formulating the research topic.

References

Abd Rahman, I. Z., Abang Hasbollah, D. Z., Mohd Yunus, N. Z., Kasiman, E. H., & Mazlan, A. N. (2022). Carbon dioxide storage potential in Malaysian sandstone aquifer: An overview. In *IOP Conference Series: Earth and Environmental Science*, (Vol. 971(1), p. 012022). https://doi.org/10.1088/1755-1315/971/1/012022

Aben, F. M., Doan, M., & Mitchell, T. M. (2020). Variation of hydraulic properties due to dynamic fracture damage: Implications for fault zones. *Journal of Geophysical Research: Solid Earth*, *125*(4), e2019JB018919. https://doi.org/10.1029/2019JB018919

Andersen, O. (2017). *Simplified models for numerical simulation of geological CO_2 storage*. [Doctoral thesis]. The University of Bergen. Retrieved from https://bora.uib.no/bora-xmlui/handle/1956/15477

Andersen, O., Gasda, S. E., & Nilsen, H. M. (2015). Vertically averaged equations with variable density for CO_2 flow in porous media. *Transport in Porous Media*, *107*(1), 95–127. https://doi.org/10.1007/s11242-014-0427-z

Andersen, O. A., Nilsen, H. M., & Gasda, S. E. (2016). Modelling geomechanical impact of CO_2 injection and migration using precomputed response functions. In *ECMOR XV—15th European Conference on the mathematics of oil recovery, Amsterdam, Netherlands*. https://doi.org/10.3997/2214-4609.201601760

Andersen, O. A., Nilsen, H. M., & Gasda, S. E. (2017). Vertical equilibrium flow models with fully coupled geomechanics for CO_2 storage modeling, using precomputed mechanical response functions. *Energy Procedia*, *114*, 3113–3131. https://doi.org/10.1016/j.egypro.2017.03.1440

Anderson, S. T. (2017). Risk, liability, and economic issues with long-term CO_2 storage—A review. *Natural Resources Research*, *26*(1), 89–112. https://doi.org/10.1007/s11053-016-9303-6

Ashworth, P., Wade, S., Reiner, D., & Liang, X. (2015). Developments in public communications on CCS. *International Journal of Greenhouse Gas Control*, *40*, 449–458. https://doi.org/10.1016/j.ijggc.2015.06.002

Bachu, S. (2008). Legal and regulatory challenges in the implementation of CO_2 geological storage: An Alberta and Canadian perspective. *International Journal of Greenhouse Gas Control*, *2*(2), 259–273. https://doi.org/10.1016/j.ijggc.2007.12.003

Ballas, G., Fossen, H., & Soliva, R. (2015). Factors controlling permeability of cataclastic deformation bands and faults in porous sandstone reservoirs. *Journal of Structural Geology*, *76*, 1–21. https://doi.org/10.1016/j.jsg.2015.03.013

Bandilla, K. W., Celia, M. A., & Leister, E. (2014). Impact of model complexity on CO_2 plume modeling at Sleipner. *Energy Procedia*, *63*, 3405–3415. https://doi.org/10.1016/j.egypro.2014.11.369

Becker, B., Guo, B., Bandilla, K., Celia, M. A., Flemisch, B., & Helmig, R. (2017). A pseudo-vertical equilibrium model for slow gravity drainage dynamics. *Water Resources Research*, *53*(12), 10491–10507. https://doi.org/10.1002/2017WR021644

Becker, B., Guo, B., Bandilla, K., Celia, M. A., Flemisch, B., & Helmig, R. (2018). An adaptive multiphysics model coupling vertical equilibrium and full multidimensions for multiphase flow in porous media. *Water Resources Research*, *54*(7), 4347–4360. https://doi.org/10.1029/2017WR022303

Becker, B., Guo, B., Buntic, I., Flemisch, B., & Helmig, R. (2022). An adaptive hybrid vertical equilibrium/full-dimensional model for compositional multiphase flow. *Water Resources Research*, *58*(1), e2021WR030990. https://doi.org/10.1029/2021WR030990

Bense, V. F., & Person, M. A. (2006). Faults as conduit-barrier systems to fluid flow in siliciclastic sedimentary aquifers. *Water Resources Research*, *42*(5), 2005WR004480. https://doi.org/10.1029/2005WR004480

Berge, R. L., Gasda, S. E., Keilegavlen, E., & Sandve, T. H. (2022). Impact of deformation bands on fault-related fluid flow in field-scale simulations. *International Journal of Greenhouse Gas Control*, *119*, 103729. https://doi.org/10.1016/j.ijggc.2022.103729

Bielicki, J. M., Pollak, M. F., Fitts, J. P., Peters, C. A., & Wilson, E. J. (2014). Causes and financial consequences of geologic CO_2 storage reservoir leakage and interference with other subsurface resources. *International Journal of Greenhouse Gas Control*, *20*, 272–284. https://doi.org/10.1016/j.ijggc.2013.10.024

Bjørnarå, T. I., Nordbotten, J. M., & Park, J. (2016). Vertically integrated models for coupled two-phase flow and geomechanics in porous media. *Water Resources Research*, *52*(2), 1398–1417. https://doi.org/10.1002/2015WR017290

Bjørnarå, T. I., Skurtveit, E., Michie, E. A. H., & Smith, S. A. (2023). Characterizing along- and across-fault fluid-flow properties for assessing flow rates and overburden fluid migration along faults: A case study from the North Sea. *Petroleum Geoscience*, *29*(3), petgeo2023-033. https://doi.org/10.1144/petgeo2023-033

Caine, J. S., Evans, J. P., & Forster, C. B. (1996). Fault zone architecture and permeability structure. *Geology*, *24*(11), 1025. https://doi.org/10.1130/0091-7613(1996)024<1025:FZAAPS>2.3.CO;2

Castelletto, N., Gambolati, G., & Teatini, P. (2013). Geological CO_2 sequestration in multi-compartment reservoirs: Geomechanical challenges. *Journal of Geophysical Research: Solid Earth*, *118*(5), 2417–2428. https://doi.org/10.1002/jgrb.50180

Celia, M. A., Bachu, S., Nordbotten, J. M., & Bandilla, K. W. (2015). Status of CO_2 storage in deep saline aquifers with emphasis on modelling approaches and practical simulations. *Water Resources Research*, *51*(9), 6846–6892. https://doi.org/10.1002/2015WR017609

Chang, K. W., & Segall, P. (2016). Injection-induced seismicity on basement faults including poroelastic stressing. *Journal of Geophysical Research: Solid Earth*, *121*(4), 2708–2726. https://doi.org/10.1002/2015JB012561

Chen, L., Elsworth, D., Chen, J., & Gan, Q. (2024). Evaluation of CO_2 leakage potential through fault instability in CO_2 geological sequestration by coupled THMC modelling. *Gas Science and Engineering*, *132*, 205486. https://doi.org/10.1016/j.jgsce.2024.205486

Childs, C., Manzocchi, T., Walsh, J. J., Bonson, C. G., Nicol, A., & Schöpfer, M. P. J. (2009). A geometric model of fault zone and fault rock thickness variations. *Journal of Structural Geology*, *31*(2), 117–127. https://doi.org/10.1016/j.jsg.2008.08.009

Choi, J. C., Skurtveit, E., Huynh, K. D. V., & Grande, L. (2023). Uncertainty of stress path in fault stability assessment during CO_2 injection: Comparing smeaheia 3D geomechanics model with analytical approaches. *International Journal of Greenhouse Gas Control*, *125*, 103881. https://doi.org/10.1016/j.ijggc.2023.103881

Class, H., Ebigbo, A., Helmig, R., Dahle, H. K., Nordbotten, J. M., Celia, M. A., et al. (2009). A benchmark study on problems related to CO_2 storage in geologic formations. *Computational Geosciences*, *13*(4), 409–434. https://doi.org/10.1007/s10596-009-9146-x

Climate Change Committee. (2021). Independent assessment: The UK'S net zero strategy. (n.d.). *Climate Change Committee*. Retrieved from https://www.theccc.org.uk/publication/independent-assessment-the-uks-net-zero-strategy/

de Jonge-Anderson, I., Ramachandran, H., Nicholson, U., Geiger, S., Widyanita, A., & Doster, F. (2024). Determining CO_2 storage efficiency within a saline aquifer using reduced complexity models. *Advances in Geo-Energy Research*, *13*(1), 22–31. https://doi.org/10.46690/ager.2024.07.04

de Jonge-Anderson, I., Widyanita, A., Busch, A., Doster, F., & Nicholson, U. (2024). New insights into the structural and stratigraphic evolution of the Malay Basin using 3D seismic data: Implications for regional carbon capture and storage potential. *Basin Research*, *36*(4), e12885. https://doi.org/10.1111/bre.12885

Dewhurst, D. N., Delle Piane, C., Esteban, L., Sarout, J., Josh, M., Pervukhina, M., & Clennell, M. B. (2018). Microstructural, geomechanical, and petrophysical characterization of shale Caprocks. In S. Vialle, J. Ajo-Franklin, & J. W. Carey (Eds.), *Geophysical monograph series* (1st ed., pp. 1–30). Wiley. https://doi.org/10.1002/9781119118657.ch1

Dixon, T., McCoy, S. T., & Havercroft, I. (2015). Legal and regulatory developments on ccs. *International Journal of Greenhouse Gas Control*, *40*, 431–448. https://doi.org/10.1016/j.ijggc.2015.05.024

Doster, F., Nordbotten, J. M., & Celia, M. A. (2012). Hysteretic upscaled constitutive relationships for vertically integrated porous media flow. *Computing and Visualization in Science*, *15*(4), 147–161. https://doi.org/10.1007/s00791-013-0206-3

Doster, F., Nordbotten, J. M., & Celia, M. A. (2013). Impact of capillary hysteresis and trapping on vertically integrated models for CO_2 storage. *Advances in Water Resources*, *62*, 465–474. https://doi.org/10.1016/j.advwatres.2013.09.005

Du Plessis, E., Nordbotten, J. M., Gasda, S. E., & Dahle, H. K. (2013). Influence of capillary pressure and trapping hysteresis on large-scale CO_2 migration. *Journal of Coupled Systems and Multiscale Dynamics*, *1*(4), 442–458. https://doi.org/10.1166/jcsmd.2013.1030

Espinoza, D. N., & Santamarina, J. C. (2017). CO_2 breakthrough—Caprock sealing efficiency and integrity for carbon geological storage. *International Journal of Greenhouse Gas Control*, *66*, 218–229. https://doi.org/10.1016/j.ijggc.2017.09.019

Fachri, M., Tveranger, J., Braathen, A., & Schueller, S. (2013). Sensitivity of fluid flow to deformation-band damage zone heterogeneities: A study using fault facies and truncated Gaussian simulation. *Journal of Structural Geology*, *52*, 60–79. https://doi.org/10.1016/j.jsg.2013.04.005

Faulkner, D. R., Jackson, C. A. L., Lunn, R. J., Schlische, R. W., Shipton, Z. K., Wibberley, C. A. J., & Withjack, M. O. (2010). A review of recent developments concerning the structure, mechanics and fluid flow properties of fault zones. *Journal of Structural Geology*, *32*(11), 1557–1575. https://doi.org/10.1016/j.jsg.2010.06.009

Gasda, S., Keilegavlen, E., Sandve, T. H., Berge, R., Pettersson, P., & Krumscheid, S. (2022). Practical field-scale simulation approaches for quantification of fault-related leakage under uncertainty. *SSRN Electronic Journal*. https://doi.org/10.2139/ssrn.4277020

Gasda, S. E., Nordbotten, J. M., & Celia, M. A. (2011). Vertically averaged approaches for CO_2 migration with solubility trapping. *Water Resources Research*, *47*(5), 2010WR009075. https://doi.org/10.1029/2010WR009075

Gasda, S. E., Stephansen, A. F., Aavatsmark, I., & Dahle, H. K. (2013). Upscaled modeling of CO_2 injection and migration with coupled thermal processes. *Energy Procedia*, *40*, 384–391. https://doi.org/10.1016/j.egypro.2013.08.044

Gibson, R. G. (1998). Physical character and fluid-flow properties of sandstone-derived fault zones. *Geological Society*, *127*(1), 83–97. https://doi.org/10.1144/GSL.SP.1998.127.01.07

Gillespie, P. A., Howard, C. B., Walsh, J. J., & Watterson, J. (1993). Measurement and characterisation of spatial distributions of fractures. *Tectonophysics*, *226*(1–4), 113–141. https://doi.org/10.1016/0040-1951(93)90114-Y

Gilmore, K. A., Sahu, C. K., Benham, G. P., Neufeld, J. A., & Bickle, M. J. (2022). Leakage dynamics of fault zones: Experimental and analytical study with application to CO_2 storage. *Journal of Fluid Mechanics*, *931*, A31. https://doi.org/10.1017/jfm.2021.970

Hasbollah, D. Z. A., Junin, R., Taib, A. M., & Mazlan, A. N. (2020). Basin evaluation of CO_2 geological storage potential in Malay basin, Malaysia. In P. Duc Long & N. T. Dung (Eds.), *Geotechnics for sustainable infrastructure development* (Vol. 62, pp. 1405–1410). Springer. https://doi.org/10.1007/978-981-15-2184-3_184

Hepple, R. P., & Benson, S. M. (2005). Geologic storage of carbon dioxide as a climate change mitigation strategy: Performance requirements and the implications of surface seepage. *Environmental Geology*, *47*(4), 576–585. https://doi.org/10.1007/s00254-004-1181-2

Herzog, H. J. (2011). Scaling up carbon dioxide capture and storage: From megatons to Gigatons. *Energy Economics*, *33*(4), 597–604. https://doi.org/10.1016/j.eneco.2010.11.004

Huppert, H. E., & Woods, A. W. (1995). Gravity-driven flows in porous layers. *Journal of Fluid Mechanics*, *292*, 55–69. https://doi.org/10.1017/S0022112095001431

Jha, B., & Juanes, R. (2014). Coupled multiphase flow and poromechanics: A computational model of pore pressure effects on fault slip and earthquake triggering. *Water Resources Research*, *50*(5), 3776–3808. https://doi.org/10.1002/2013WR015175

Jones, D. G., Beaubien, S. E., Blackford, J. C., Foekema, E. M., Lions, J., De Vittor, C., et al. (2015). Developments since 2005 in understanding potential environmental impacts of CO_2 leakage from geological storage. *International Journal of Greenhouse Gas Control*, *40*, 350–377. https://doi.org/10.1016/j.ijggc.2015.05.032

Kang, M., Nordbotten, J. M., Doster, F., & Celia, M. A. (2014). Analytical solutions for two-phase subsurface flow to a leaky fault considering vertical flow effects and fault properties. *Water Resources Research*, *50*(4), 3536–3552. https://doi.org/10.1002/2013WR014628

Kettermann, M., Smeraglia, L., Morley, C. K., Von Hagke, C., & Tanner, D. C. (2020). Fault sealing. In *Understanding faults* (pp. 283–350). Elsevier. https://doi.org/10.1016/B978-0-12-815985-9.00008-4

Knipe, R. J., Jones, G., & Fisher, Q. J. (1998). Faulting, fault sealing and fluid flow in hydrocarbon reservoirs: An introduction. *Geological Society, London, Special Publications*, *147*(1). https://doi.org/10.1144/GSL.SP.1998.147.01.01

Krevor, S., De Coninck, H., Gasda, S. E., Ghaleigh, N. S., De Gooyert, V., Hajibeygi, H., et al. (2023). Subsurface carbon dioxide and hydrogen storage for a sustainable energy future. *Nature Reviews Earth & Environment*, *4*(2), 102–118. https://doi.org/10.1038/s43017-022-00376-8

Kumar, A., Ozah, R., Noh, M., Pope, G. A., Bryant, S., Sepehrnoori, K., & Lake, L. W. (2005). Reservoir simulation of CO_2 storage in deep saline aquifers. *SPE Journal*, *10*(3), 336–348. https://doi.org/10.2118/89343-PA

Lie, K.-A. (2019). *An introduction to reservoir simulation using matlab/gnu octave: User guide for the matlab reservoir simulation toolbox(Mrst)* (1st ed.). Cambridge University Press. https://doi.org/10.1017/9781108591416

Madon, M., & Department of Geology, & Universiti Malaya, 50603 Kuala Lumpur, Malaysia. (2021). Five decades of petroleum exploration and discovery in the Malay basin (1968–018) and remaining potential. *Bulletin Geological Society of Malaysia*, *72*, 63–88. https://doi.org/10.7186/bgsm72202106

Madon, M., & Jong, J., & JX Nippon Oil and Gas Exploration (Malaysia) Limited, Malaysia. Malaysian Continental Shelf Project, National Security Council, Malaysia. (2021). Geothermal gradient and heat flow maps of offshore Malaysia: Some updates and observations. *Bulletin Geological Society of Malaysia*, *71*, 159–183. https://doi.org/10.7186/bgsm71202114

Manzocchi, T., Childs, C., & Walsh, J. J. (2010). Faults and fault properties in hydrocarbon flow models. *Geofluids*, *10*(1–2), 94–113. https://doi.org/10.1111/j.1468-8123.2010.00283.x

Manzocchi, T., Walsh, J. J., Nell, P., & Yielding, G. (1999). Fault transmissibility multipliers for flow simulation models. *Petroleum Geoscience*, *5*(1), 53–63. https://doi.org/10.1144/petgeo.5.1.53

Meguerdijian, S., & Jha, B. (2021). Quantification of fault leakage dynamics based on leakage magnitude and dip angle. *International Journal for Numerical and Analytical Methods in Geomechanics*, *45*(16), 2303–2320. https://doi.org/10.1002/nag.3267

Michie, E. A. H., Mulrooney, M. J., & Braathen, A. (2021). Fault interpretation uncertainties using seismic data, and the effects on fault seal analysis: A case study from the Horda platform, with implications for CO_2; storage. *Solid Earth*, *12*(6), 1259–1286. https://doi.org/10.5194/se-12-1259-2021

Mitchell, T. M., & Faulkner, D. R. (2012). Towards quantifying the matrix permeability of fault damage zones in low porosity rocks. *Earth and Planetary Science Letters*, *339–340*, 24–31. https://doi.org/10.1016/j.epsl.2012.05.014

Møyner, O., & Nilsen, H. M. (2019). Multiresolution coupled vertical equilibrium model for fast flexible simulation of CO_2 storage. *Computational Geosciences*, *23*(1), 1–20. https://doi.org/10.1007/s10596-018-9775-z

Neufeld, J. A., Vella, D., & Huppert, H. E. (2009). The effect of a fissure on storage in a porous medium. *Journal of Fluid Mechanics*, *639*, 239–259. https://doi.org/10.1017/S0022112009991030

Nilsen, H., Herrera, P. A., Ashraf, M., Ligaarden, I., Iding, M., Hermanrud, C., et al. (2011). Field-case simulation of CO_2 -plume migration using vertical-equilibrium models. *Energy Procedia*, *4*, 3801–3808. https://doi.org/10.1016/j.egypro.2011.02.315

Nilsen, H., Lie, K.-A., & Andersen, O. (2015). Analysis of CO_2 trapping capacities and long-term migration for geological formations in the Norwegian North Sea using MRST-CO_2lab. *Computers & Geosciences*, *79*, 15–26. https://doi.org/10.1016/j.cageo.2015.03.001

Nilsen, H. M., Lie, K.-A., & Andersen, O. (2016). Fully-implicit simulation of vertical-equilibrium models with hysteresis and capillary fringe. *Computational Geosciences*, *20*(1), 49–67. https://doi.org/10.1007/s10596-015-9547-y

Nilsen, H. M., Lie, K.-A., & Andersen, O. (2016). Robust simulation of sharp-interface models for fast estimation of CO_2 trapping capacity in large-scale aquifer systems. *Computational Geosciences*, *20*(1), 93–113. https://doi.org/10.1007/s10596-015-9549-9

Nordbotten, J. M., & Celia, M. A. (2011). *Geological storage of CO_2: Modeling approaches for large-scale simulation* (1st ed.). Wiley. https://doi.org/10.1002/9781118137086

Nordbotten, J. M., & Dahle, H. K. (2011). Impact of the capillary fringe in vertically integrated models for CO_2 storage. *Water Resources Research*, *47*(2), 2009WR008958. https://doi.org/10.1029/2009WR008958

Oladyshkin, S., Class, H., Helmig, R., & Nowak, W. (2011). A concept for data-driven uncertainty quantification and its application to carbon dioxide storage in geological formations. *Advances in Water Resources*, *34*(11), 1508–1518. https://doi.org/10.1016/j.advwatres.2011.08.005

Pawar, R. J., Bromhal, G. S., Carey, J. W., Foxall, W., Korre, A., Ringrose, P. S., et al. (2015). Recent advances in risk assessment and risk management of geologic CO_2 storage. *International Journal of Greenhouse Gas Control*, *40*, 292–311. https://doi.org/10.1016/j.ijggc.2015.06.014

Pawar, R. J., Bromhal, G. S., Chu, S., Dilmore, R. M., Oldenburg, C. M., Stauffer, P. H., et al. (2016). The national risk assessment Partnership's integrated assessment model for carbon storage: A tool to support decision making amidst uncertainty. *International Journal of Greenhouse Gas Control*, *52*, 175–189. https://doi.org/10.1016/j.ijggc.2016.06.015

Pei, Y., Paton, D. A., Knipe, R. J., & Wu, K. (2015). A review of fault sealing behaviour and its evaluation in siliciclastic rocks. *Earth-Science Reviews*, *150*, 121–138. https://doi.org/10.1016/j.earscirev.2015.07.011

Petrie, E. S., Petrie, R. A., & Evans, J. P. (2014). Identification of reactivation and increased permeability associated with a fault damage zone using a multidisciplinary approach. *Journal of Structural Geology*, *59*, 37–49. https://doi.org/10.1016/j.jsg.2013.11.008

Pettersson, P., Keilegavlen, E., Sandve, T. H., Gasda, S. E., & Krumscheid, S. (2025). Copula modeling and uncertainty propagation in field-scale simulation of CO_2 fault leakage. *Water Resources Research*, *61*(1), e2024WR038073. https://doi.org/10.1029/2024WR038073

Phillips, T., Kampman, N., Bisdom, K., Forbes Inskip, N. D., Den Hartog, S. A. M., Cnudde, V., & Busch, A. (2020). Controls on the intrinsic flow properties of Mudrock fractures: A review of their importance in subsurface storage. *Earth-Science Reviews*, *211*, 103390. https://doi.org/10.1016/j.earscirev.2020.103390

Pruess, K. (2011). Integrated modeling of CO_2 storage and leakage scenarios including transitions between super- and subcritical conditions, and phase change between liquid and gaseous CO_2. *Greenhouse Gases: Science and Technology*, *1*(3), 237–247. https://doi.org/10.1002/ghg.24

Ramachandran, H. (2025). Poriyalar/Faultve: Faultve (v1.0) [Software]. *Zenodo*. https://doi.org/10.5281/zenodo.17469206

Ramachandran, H., Pope, G. A., & Srinivasan, S. (2017). Numerical study on the effect of thermodynamic phase changes on CO_2 leakage. *Energy Procedia*, *114*, 3528–3536. https://doi.org/10.1016/j.egypro.2017.03.1482

Rinaldi, A. P., Rutqvist, J., & Cappa, F. (2014). Geomechanical effects on CO_2 leakage through fault zones during large-scale underground injection. *International Journal of Greenhouse Gas Control*, *20*, 117–131. https://doi.org/10.1016/j.ijggc.2013.11.001

Ringrose, P., & Bentley, M. (2021). *Reservoir model design: A practitioner's guide*. Springer International Publishing. https://doi.org/10.1007/978-3-030-70163-5

Ringrose, P. S., & Meckel, T. A. (2019). Maturing global CO_2 storage resources on offshore continental margins to achieve 2DS emissions reductions. *Scientific Reports*, *9*(1), 17944. https://doi.org/10.1038/s41598-019-54363-z

Rizzo, R. E., Inskip, N. F., Fazeli, H., Betlem, P., Bisdom, K., Kampman, N., et al. (2024). Modelling geological CO_2 leakage: Integrating fracture permeability and fault zone outcrop analysis. *International Journal of Greenhouse Gas Control*, *133*, 104105. https://doi.org/10.1016/j.ijggc.2024.104105

Romanak, K., & Dixon, T. (2022). CO_2 storage guidelines and the science of monitoring: Achieving project success under the California low carbon fuel standard CCS protocol and other global regulations. *International Journal of Greenhouse Gas Control*, *113*, 103523. https://doi.org/10.1016/j.ijggc.2021.103523

Rutqvist, J. (2012). The geomechanics of CO_2 storage in deep sedimentary formations. *Geotechnical & Geological Engineering*, *30*(3), 525–551. https://doi.org/10.1007/s10706-011-9491-0

Saló-Salgado, L., Davis, S., & Juanes, R. (2023). Fault permeability from stochastic modeling of clay smears. *Geology*, *51*(1), 91–95. https://doi.org/10.1130/G50739.1

Sayag, R., & Neufeld, J. A. (2016). Propagation of viscous currents on a porous substrate with finite capillary entry pressure. *Journal of Fluid Mechanics*, *801*, 65–90. https://doi.org/10.1017/jfm.2016.412

Seebeck, H., Nicol, A., Walsh, J. J., Childs, C., Beetham, R. D., & Pettinga, J. (2014). Fluid flow in fault zones from an active rift. *Journal of Structural Geology*, *62*, 52–64. https://doi.org/10.1016/j.jsg.2014.01.008

Sibson, R. H. (1977). Fault rocks and fault mechanisms. *Journal of the Geological Society*, *133*(3), 191–213. https://doi.org/10.1144/gsjgs.133.3.0191

Silva, J. A., Saló-Salgado, L., Patterson, J., Dasari, G. R., & Juanes, R. (2023). Assessing the viability of CO_2 storage in offshore formations of the Gulf of Mexico at a scale relevant for climate-change mitigation. *International Journal of Greenhouse Gas Control*, *126*, 103884. https://doi.org/10.1016/j.ijggc.2023.103884

Simpson, G., Guéguen, Y., & Schneider, F. (2001). Permeability enhancement due to microcrack dilatancy in the damage regime. *Journal of Geophysical Research*, *106*(B3), 3999–4016. https://doi.org/10.1029/2000JB900194

Smith, D. A. (1980). Sealing and nonsealing faults in Louisiana gulf coast salt basin. *AAPG Bulletin*, *64*(2), 145–172. https://doi.org/10.1306/2F918946-16CE-11D7-8645000102C1865D

Snippe, J., Kampman, N., Bisdom, K., Tambach, T., March, R., Maier, C., et al. (2022). Modelling of long-term along-fault flow of CO_2 from a natural reservoir. *International Journal of Greenhouse Gas Control*, *118*, 103666. https://doi.org/10.1016/j.ijggc.2022.103666

Tewari, R. D., Tan, C. P., & Sedaralit, M. F. (2023). A toolkit approach for carbon capture and storage in offshore depleted gas field. *American Journal of Environmental Sciences*, *19*(1), 8–42. https://doi.org/10.3844/ajessp.2023.8.42

Tueckmantel, C., Fisher, Q. J., Manzocchi, T., Skachkov, S., & Grattoni, C. A. (2012). Two-phase fluid flow properties of cataclastic fault rocks: Implications for CO_2 storage in saline aquifers. *Geology*, *40*(1), 39–42. https://doi.org/10.1130/G32508.1

Vilarrasa, V., Makhnenko, R. Y., & Laloui, L. (2017). Potential for fault reactivation due to CO_2 injection in a semi-closed saline aquifer. *Energy Procedia*, *114*, 3282–3290. https://doi.org/10.1016/j.egypro.2017.03.1460

Walsh, J. J., Watterson, J., Heath, A. E., & Childs, C. (1998). Representation and scaling of faults in fluid flow models. *Petroleum Geoscience*, *4*(3), 241–251. https://doi.org/10.1144/petgeo.4.3.241

Yielding, G., Bretan, P., & Freeman, B. (2010). Fault seal calibration: A brief review. *Geological Society, London, Special Publications*, *347*(1), 243–255. https://doi.org/10.1144/SP347.14

Yielding, G., Freeman, B., & Needham, D. T. (1997). Quantitative fault seal prediction. *AAPG Bulletin*, *81*(1997), 897–917. https://doi.org/10.1306/522B498D-1727-11D7-8645000102C1865D

Yortsos, Y. C. (1995). A theoretical analysis of vertical flow equilibrium. *Transport in Porous Media*, *18*(2), 107–129. https://doi.org/10.1007/BF01064674

Zhao, X., & Jha, B. (2019). Role of well operations and multiphase geomechanics in controlling fault stability during CO_2 storage and enhanced oil recovery. *Journal of Geophysical Research: Solid Earth*, *124*(7), 6359–6375. https://doi.org/10.1029/2019JB017298

Zheng, X., & Espinoza, D. N. (2022). Stochastic quantification of CO_2 fault sealing capacity in sand-shale sequences. *Marine and Petroleum Geology*, *146*, 105961. https://doi.org/10.1016/j.marpetgeo.2022.105961